CO2 conversion into hydrocarbons via modified Fischer-Tropsch synthesis by using bulk iron catalysts combined with zeolites

Available online at www.sciencedirect.com

Chemical Engineering Research and Design

journal homepage: www.elsevier.com/locate/cherd

CO_2 conversion into hydrocarbons via modified Fischer-Tropsch synthesis by using bulk iron catalysts combined with zeolites

Elena Corrao[a], *Fabio Salomone*[a,*], *Emanuele Giglio*[b], *Micaela Castellino*[a], *Silvia Maria Ronchetti*[a], *Marco Armandi*[a], *Raffaele Pirone*[a], *Samir Bensaid*[a]

[a] *Department of Applied Science and Technology (DISAT), Politecnico di Torino, Corso Duca degli Abruzzi 24, 10129 Torino, Italy*

[b] *Chemical Engineering and Catalysis for Sustainable Processes (CECaSP) Laboratory, University of Calabria, Via Pietro Bucci, 87036 Rende, Italy*

ARTICLE INFO

Article history:
Received 31 May 2023
Received in revised form 31 July 2023
Accepted 31 July 2023
Available online 2 August 2023

Keywords:
CO_2 hydrogenation
Modified Fischer-Tropsch
Core-shell structures
Liquid fuel
Fe-based catalyst

ABSTRACT

To effectively address the challenges posed by global warming, a prompt and coordinated effort is necessary to conduct an extensive study aimed at reducing CO_2 emissions and overcoming the obstacles presented by expensive and scarce fossil fuel resources. This study primarily focuses on comparing two different methodologies for preparing Na-promoted Fe_3O_4-based catalysts for the CO_2 hydrogenation into hydrocarbon mixtures. Three catalysts were synthesized and tested: two samples were impregnated with a different amount of Na (1 wt% and 5 wt%), while a third one was obtained via coprecipitation with NaOH. As the latter catalyst exhibited the best performance, it was combined with zeolites in two ways: physical mixtures and core-shell structures. MFI-type zeolites were used in both configurations and a conventional structure was compared to a hierarchical one. As a result, mesopores increased successfully both the CO_2 conversion from 37% to 40% and the liquid hydrocarbon (C_{6+}) selectivity from 29% to 57%, doubling the C_{6+} yield. On the other hand, NH_3-TPD and XPS measurements demonstrated that the intimate contact between the two materials in the core-shell structures led to the migration of Na from the oxide to the zeolite reducing the concentration of strong acid sites and, consequently, the liquid hydrocarbon yield.

1. Introduction

Petroleum industry has promoted economic development and societal well-being. On the other hand, the massive and growing dependence on fossil fuels has led to an uncontrolled increase in CO_2 emissions. International Energy Agency (IEA) estimated that CO_2 emissions have increased by more than 40% compared to pre-industrial levels (from 280 ppm to values above 400 ppm) (Energy Agency, I. 2021; Yang et al., 2022). The most serious consequence related to increasing greenhouse gas emissions is the average temperature rise, which implies an increase in sea level, ocean acidification, and climate change with increasingly frequent disastrous effects. Furthermore, fossil fuels are subject to fluctuations in supply and crude oil prices due to global geopolitical reasons (Lin et al., 2022). Finally, being

* Corresponding author.
E-mail address: fabio.salomone@polito.it (F. Salomone).

https://doi.org/10.1016/j.cherd.2023.07.052

Nomenclature

Acronyms and Abbreviations

AIP	Aluminum isopropoxide
ASF	Anderson-Schulz-Flory
EDS	Energy Dispersion X-ray Spectroscopy
FE-SEM	Field-emission Scanning Electron Microscopy
FIB	Focused Ion Beam
FID	Flame Ionization Detector
FTS	Fischer Tropsch Synthesis
GC	Gas Chromatography
HPLC	High Performance Liquid Chromatography
HR	High Resolution
IEA	International Energy Agency
MS	Mass Spectrometry
NDIR	Nondispersive infrared
RWGS	Reverse Water Gas Shift
TCD	Thermal Conductivity Detector
TEM	Transmission Electron Microscopy
TEOS	Tetraethyl orthosilicate
TOC	Total Organic Carbon
TOS	Time-on-stream
TPAOH	Tetrapropylammonium hydroxide
TPC	Temperature Programmed Combustion
TPD	Temperature Programmed Desorption
TPR	Temperature Programmed Reduction
XPS	X-ray Photoelectron Spectroscopy
XRD	X-ray Diffraction analysis
XRF	X-ray Fluorescence Spectroscopy

Parameters

ζ_{CO_2}	CO_2 conversion (dimensionless)
$\dot{n}_{CO_2,conv}$	molar flow rate carbon dioxide converted ($mol \cdot s^{-1}$)
$\dot{n}_{CO_2,in}$	inlet carbon dioxide molar flow rate ($mol \cdot s^{-1}$)
$\dot{n}_{CO_2,out}$	outlet carbon dioxide molar flow rate ($mol \cdot s^{-1}$)
σ_i	selectivity (dimensionless)
$\dot{n}_{C,i,out}$	outlet carbon molar flow rate for the i-th chemical species ($mol \cdot s^{-1}$)
$N_{C,i}$	number of carbon atoms of the i-th chemical species (dimensionless)
$\dot{n}_{i,out}$	outlet molar flow rate of the i-th compound ($mol \cdot s^{-1}$)
OS_j	olefinic share (dimensionless)
$\dot{n}_{j,O}$	molar flow rate of the j-th olefinic group between C_2 and C_5 ($mol \cdot s^{-1}$)
$\dot{n}_{j,P}$	molar flow rate of the j-th paraffinic group between C_2 and C_5 ($mol \cdot s^{-1}$)
$\dot{n}_{out}$	total outlet molar flow rate ($mol \cdot s^{-1}$)
$\dot{n}_{in}$	total inlet molar flow rate (mol·s-1)
$y_{N_2,in}$	outlet nitrogen molar fraction (dimensionless)
$y_{N_2,out}$	inlet nitrogen molar fraction (dimensionless)

non-renewable sources of energy, they are destined to run out over time.

CO_2 could be captured and converted into fuels or high-value chemical products via reaction with green hydrogen produced by exploiting surpluses from renewable energy sources (Giglio et al., 2021a, 2021b; Parigi et al., 2019), in order to embark on a sustainable pathway to produce synthetic fuels like methane (Power-to-Gas) (Giglio et al., 2021a; Mazza et al., 2020; Salomone et al., 2019), methanol (Guzmán et al., 2022, 2021; Salomone et al., 2023b), dimethyl-ether (Dieterich et al., 2020; Salomone et al., 2022) and hydrocarbons (Power-to-Liquid) (Gambo et al., 2022; Numpilai et al., 2021; Ojelade and Zaman, 2021; Panzone et al., 2020; Salomone et al., 2023a; Wang et al., 2019).

The conversion of CO_2 is a challenging process due to its stability (Gao et al., 2018). Therefore, the development of an efficient catalyst for CO_2 conversion is highly desirable. In this context, conventional Fischer-Tropsch synthesis (FTS) Fe-, Co-, Ni-, and Ru-based catalysts (Dieterich et al., 2020; Panzone et al., 2020; Perego et al., 2009; Sharma et al., 2021), have been studied for CO_2 hydrogenation to hydrocarbons. Among them, Ni- and Ru-based catalysts show high CH_4 efficiency (Marocco et al., 2018; Porta et al., 2020), but only small amounts of C_{2+} hydrocarbons are produced.

Power-to-Liquid is a good candidate for medium-term energy storage. Liquid products are easy to transport and store (whereas gaseous products require compression or liquefaction), having a higher energy density per unit volume and experiencing less material losses during long-term storage. Liquid fuels are compatible with the existing infrastructure, making their integration into an industrial sector relatively straightforward without requiring extensive investments or technological overhauls.

Indirect or direct routes can be carried out for the CO_2 hydrogenation into liquid fuels, as schematized in Fig. 1. The indirect route requires the use of two separate reactors. In the first one CO_2 and H_2 can be firstly converted into CH_3OH or CO (depending on the catalyst), that are subsequently transformed into hydrocarbons within a second step/reactor. On the other hand, the direct route may be more economically advantageous than the indirect one thanks to the use of a unique reactor. The direct conversion process consists of coupling between the endothermic reverse water gas shift (RWGS) reaction and the exothermic Fischer-Tropsch synthesis (FTS) within the same catalytic particle. In the direct pathways, CO_2 is converted into CO via the RWGS reaction according to Eq. (1), followed by its hydrogenation into hydrocarbons via Fischer-Tropsch synthesis (FTS) as reported in Eqs. (2) and (3) (De Klerk, 2014; Liang et al., 2019; Sharma et al., 2021). This process is generally known as modified Fischer-Tropsch synthesis (Fig. 1) (Gao et al., 2018; Panzone et al., 2020); the main products are olefins, paraffins and naphthenes, but some oxygenates are by-products such as alcohols, carboxylic acids and aldehydes.

$$CO_2 + H_2 \rightleftharpoons CO + H_2O \qquad \Delta\tilde{H}^0_{298K} = +41 kJ\ mol^{-1} \tag{1}$$

$$n\ CO + 2n\ H_2 \rightarrow C_nH_{2n} + n\ H_2O \tag{2}$$

$$n\ CO + (2n+1)H_2 \rightarrow C_nH_{2n+2} + n\ H_2O \tag{3}$$

Fe-based catalysts have been studied extensively for their high activity and stability in hydrocarbons production (Jiang et al., 2023). They are particularly attractive due to their potential in directly converting CO_2 into fuels. This feature is due to the formation of carbides, helping the reduction of Fe_3O_4 catalyst. CO_2 is firstly reduced into CO on the iron oxide sites via RWGS, as reported in Eq. (1), followed by the carbon hydrogenation on Fe_5C_2 sites to form -CH_2- groups as chain initiators and monomer units for the chain growth (FTS), as reported in Eqs. (2) and (3) (Liu et al., 2018). To achieve high selectivity of light olefins, the carbon chain growth reaction needs to be effectively controlled (Liang et al., 2019). Therefore,

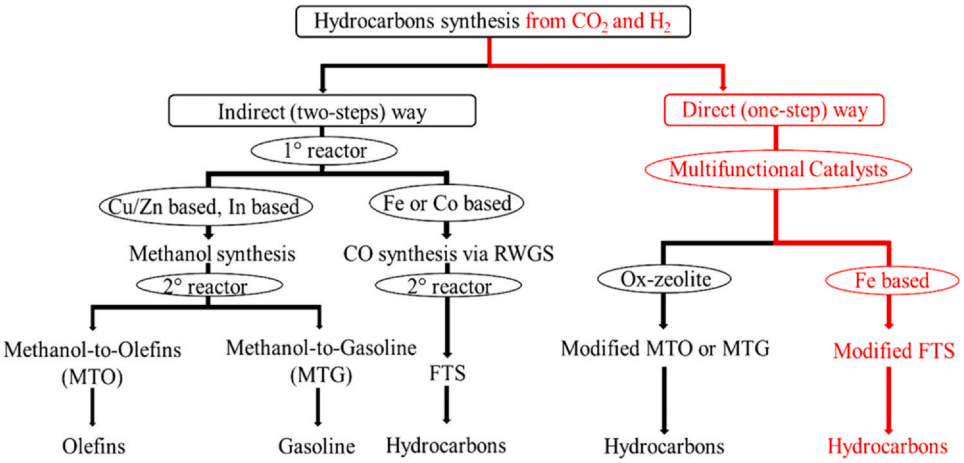

Fig. 1 – Different ways to hydrogenate CO_2 to hydrocarbon final products.

efforts are still underway to improve the catalytic performance of Fe-based catalysts by incorporating promoters. Among them, the addition of alkali promoters such as Na or K significantly enhances the formation of Fe_5C_2 sites and reduces methane production, promoting the olefins selectivity.

Zeolites are a crucial components of tandem catalysts in both the discussed routes for CO_2 hydrogenation (Fig. 1), as they possess unique shape selectivity and acidity enabling hydrocarbons oligomerization, isomerization, and aromatization. ZSM-5 with MFI topology is the most preferred catalyst candidate for aromatic synthesis among the solid acids used in the process because of its well-defined 3-dimensional intersecting pore system with 10-member ring channels. This feature allows it to surmount the challenges of reactant and product diffusion within the pores and maintain strong resistance to deactivation by coke. Besides zeolite topology, type, strength, and concentration of acid sites, as well as, and Si/Al atomic ratio and pore size distribution are critical factors in determining the catalyst effectiveness (Wei et al., 2021, 2017).

If a zeolite is involved, lower olefins may undergo oligomerization (according to the hydrogen transfer mechanism) to produce olefins in the C_6-C_{10} range. Subsequently, the longer olefins can transfer their hydrogen to another olefin molecule, leading to the generation of dienes and paraffins. The dienes then form cyclic olefins via cyclization and undergo two hydrogen transfer steps, producing cyclic dienes and aromatics, as reported in the simplified Eq. (4). The occurrence of each hydrogen transfer step results in the formation of one paraffin molecule, which reduces the carbon utilization in terms of producing the desired chemicals (C_2-C_4 olefins and aromatics) (Weber et al., 2018; Wei et al., 2017; Song et al., 2022; Xu et al., 2018; Wang et al., 2021; Cui et al., 2019). Organic oxygen compounds obtained on the Fe-based catalyst, especially alcohols and ethers, can react on the acid sites of the zeolite, following the reaction pathway reported in the Eqs. (5) and (6). Eqs. (5) and (6) can lead to the formation of paraffins and olefins, respectively (Fuhse and Bandermann, 1987). The latter may undergo further conversion to aromatic products on the acidic sites of the zeolite as previously mentioned. The capability of zeolite to transform light olefins and alcohols intermediate products depends on the strongness of acid sites of the zeolite.

$$C_nH_{2n} \rightarrow \frac{1}{m}C_6H_6 + \frac{3}{m}C_nH_{2n+2}, \text{ where: } m = \frac{6}{n} + 3 \quad (4)$$

$$C_nH_{2n+2}O \rightarrow C_nH_{2n+2} + H_2O + C \quad (5)$$

$$C_nH_{2n+2}O \rightarrow C_nH_{2n} + H_2O \quad (6)$$

Zeolites with low Si/Al atomic ratio (lower than 10) could cause the over-cracking of heavy hydrocarbons due to their high acidity, leading to a decrease in selectivity towards liquid hydrocarbons in FT synthesis. On the contrary, zeolites with a high Si/Al ratio (greater than 100) are characterized by a lower concentration of acid sites, which is not beneficial for the oligomerization, isomerization, and aromatization of primary CO_2-FT products. HZSM-5 with a medium number of acid sites gives the possibility to obtain a gasoline-like product (Wei et al., 2017).

Therefore, the Si/Al atomic ratio for zeolites used in FT synthesis ranges typically between 40 and 80, which provides a balance between activity, selectivity, and stability of the catalyst. However, the optimal Si/Al ratio depends on the specific reaction conditions and the type of syngas used in the process. Due to its larger average pore size, a hierarchical zeolite is able to enhance mass transport by enabling faster movement of reactant and product molecules through the catalyst, resulting in improved catalytic activity and selectivity. Additionally, the mesopores present in hierarchical zeolites offer better accessibility to active sites for intermediate products, thereby enhancing catalytic performance in reactions involving larger molecules. Moreover, the presence of mesopores helps to mitigate the diffusion limitations that can lead to catalyst deactivation in conventional zeolites (Wei et al., 2021, 2017).

According to previous research works, capsule catalysts with a core-shell structure have demonstrated remarkable performance for FTS. The combination of the core and shell seems to produce a synergistic confinement effect, enabling to break the Anderson-Schulz-Flory (ASF) distribution and achieve high selectivity for the desired products. By carefully selecting and optimizing the materials used for the core and shell, these bifunctional capsule catalysts can outperform physical mixtures (Ma et al., 2020; Song et al., 2022). Overall, efforts to improve the catalytic performance of Fe-based catalysts and optimize their configuration to lead to the development of more efficient and selective processes for converting CO_2 into valuable fuels require further studies.

Therefore, the aim of this work is to investigate and optimize the catalysts for the hydrogenation of CO_2 into hydrocarbons. Hence, multifunctional materials made of a Fe-based metal oxide with Na as promoter, (prepared according

to two different synthesis and with different amount of Na) were studied. Subsequently, the best metallic phase was tested in physical mixture mode with two MFI zeolites. A commercial and an homemade hierarchical one with a Si/Al atomic ratio of 40 was chosen in order to have a good compromise in terms of performances and production of gasoline-like products.

To specify the principal objective of this study is to comprehensively compare hierarchical zeolite with conventional zeolite, focusing specifically on the impact of zeolite morphology. The results have highlighted the superior activity of the synthesized hierarchical zeolite in comparison to the non-mesoporous zeolite structure.

Furthermore, in this work, in-situ X-ray diffraction (XRD) measurements were carried out under non-ambient conditions, providing crucial information about the catalyst's reducibility and the reaction mechanism.

Moreover, this research seeks to prepare and test two distinct structures using the cladding method, inspired by previous studies, to investigate their potential in improving selectivity towards desired products. Specifically, the objective is to enhance selectivity towards target products (such as gasoline) through a complete conversion of olefins, which are obtained on the active sites of Na-Fe_3O_4 and act as reaction intermediates over the acidic sites of a zeolite. In addition to a conventional zeolite, a homemade hierarchical zeolite was employed, leveraging its mesoporous structure to improve the mass transfer efficiency of intermediates during the catalytic process (Wang et al., 2020).

Additionally, this study delves into a detailed analysis of sodium migration, a topic extensively discussed in the literature but relatively neglected from a catalytic perspective.

By building upon existing concepts and introducing novel insights, this research work endeavors to contribute to the advancement of state-of-the-art multifunctional catalysts, validated through conventional characterizations and stability tests.

2. Material and methods

2.1. Catalyst preparation

2.1.1. Impregnation of Fe_3O_4 with Na

Fe_3O_4 was prepared by adding 6 g of $FeCl_2{\cdot}4\,H_2O$, 8.6 g of $FeCl_3$ and 125 mL of milli-Q water to a 250 mL three-neck round bottom flask and vigorously stirring the system for 30 min under a nitrogen atmosphere at 90 °C. Then, 45 mL of ammonium hydroxide solution (NH_3, 28 wt%) were rapidly added. The mixture turned black, and the reaction was kept at 90 °C for 3 h. At this point, the product was magnetically separated, washed with milli-Q water until pH neutrality and dried at 60 °C overnight (Zhong et al., 2019). Finally, the obtained Fe_3O_4 was impregnated with the desired amount of sodium as promoter using the wet impregnation method. Specifically, 185 mg of $NaNO_3$ were mixed with 5.0 mL of H_2O in a beaker, then 5.0 g of pure Fe_3O_4 were added. The suspension was sonicated for 30 min and left to stand for 4 h. This procedure was repeated three times. The solvent was evaporated, and the sample was dried at 60 °C overnight. Then, the sample was calcined under air at 400 °C for 4 h (heating rate: 5 °C·min^{-1}). The sample was named as '1%Na-Fe_3O_4_WI'. A similar procedure was followed for a second sample labelled '5%$NaFe_3O_4$_WI', obtained by adjusting the amount of $NaNO_3$ (Wen et al., 2020). (%Na nominal content is intended as g_{Na}/g_{Fe3O4}).

2.1.2. $NaFe_3O_4$ obtained by coprecipitation with NaOH

A $NaFe_3O_4$ catalyst was synthesized by a one-pot synthesis method. A proper mass of iron chlorides (18.98 g of $FeCl_3$ and 12.54 g of $FeCl_2{\cdot}4\,H_2O$) was dissolved in 5.1 mL of HCl (12.1 mol·L^{-1}), and finally 150 mL of water were added. Then, NaOH (1.5 mol·L^{-1}) was added dropwise to the solution under stirring at 60 °C until the pH of the final solution was maintained at ≈ 10. After continuously stirring for 1 h, the black-brown product was separated by a magnet and washed with 800 mL of deionized water (Wei et al., 2017). The washed nanoparticles were dried overnight at 60 °C and hereafter denoted as '$NaFe_3O_4$_CP'.

2.1.3. Synthesis of hierarchical zeolite

Besides a commercial HZSM-5 zeolite having a Si/Al atomic ratio of 40, a homemade hierarchical zeolite having the same Si/Al theoretical atomic ratio was prepared via hydrothermal synthesis and labelled as 'HZ'. To specify, an aqueous solution containing 29.2 g of tetraethyl orthosilicate (TEOS), 0.75 g of aluminum isopropoxide (AIP), 13 g of tetrapropylammonium hydroxide (TPAOH, 40 wt% in water), and 68 mL of water was prepared in a flask, and the mixture was stirred at room temperature for 30 min. Then, the solution was recrystallized under reflux with stirring at 90 °C for 20 h. Subsequently, 1.20 g of 3-aminopropyltrimethoxysilane (3-APTMS, 97%) was added to the solution, and the mixture was stirred for 6 h again at 90 °C. The precursor ZSM-5 zeolite solution was crystallized in a Teflon-lined stainless-steel autoclave at 170 °C for 5 days. Thereafter, the precipitate was separated by centrifuge and washed with water. After being dried overnight at 60 °C the sample was calcined at 550 °C for 5 h (Wen et al., 2020).

2.1.4. Physical mixture

Physical mixtures of the Na-containing Fe_3O_4 active phases for CO_2 hydrogenation were mixed with a zeolite (either commercial HZSM-5 or homemade hierarchical HZ) to perform the one-pot FTS. The samples were prepared by mixing pellets (sieved in the range 300–500 μm) of Na-Fe_3O_4 catalysts and zeolites in a mass ratio of 1:1. The obtained mixtures were labelled as '$NaFe_3O_4$_CP+HZSM5′ and '$NaFe_3O_4$_CP+HZ'.

2.1.5. Core-shell structures

The metallic phase prepared via coprecipitation ($NaFe_3O_4$_CP) was selected to assess its close interaction with the zeolite in terms of diffusional phenomena of reactants and products, as well as of the Na mobility. Thus, two core-shell catalysts (labelled as '$NaFe_3O_4$_CP@HZSM5′ and '$NaFe_3O_4$_CP@HZ') were synthetized by means of a physically adhesive technique (Song et al., 2022).

$NaFe_3O_4$_CP@HZSM-5 was prepared mixing 2 g of $NaFe_3O_4$ particles (sieved to a range of 300–500 μm), with 0.5 g of LUDOX (aqueous solution with 30 wt% of SiO_2) diluted with 2 mL of milli-Q water. Subsequently, 2 g of commercial HZSM-5 (Si/Al=40) powder were manually added to the moist granules. The obtained pellets were transferred in a round-bottom flask and kept under rotation for 2 h to dry the mixture. Then, the core-shell pellets were calcined at 400 °C for 3 h (heating rate: 2.5 °C·min^{-1}).

$NaFe_3O_4$_CP@HZ was prepared with the same active phase of $NaFe_3O_4$_CP@HZSM-5 but using HZ zeolite (in its 'as

made' form, i.e., with pores still filled with the structure directing agent) as shell instead of commercial HZSM-5. Once the core-shell structure was obtained, $NaFe_3O_4$_CP@HZ pellets were heated up to 550 °C at a heating rate of 2 °C·min^{-1} for 3 h to decompose the organic template.

2.2. Catalysts characterization

Structural characterization of the fresh and spent catalysts was carried out through the following techniques: N_2 physisorption, X-ray fluorescence (XRF), field-emission scanning electron microscopy (FE-SEM), transmission electron microscopy (TEM), energy-dispersive X-ray spectroscopy (EDS), temperature-programmed measurements (H_2-TPR, CO_2-TPD, NH_3-TPD and TPC), X-ray photoelectron spectroscopy (XPS) and X-ray diffraction (XRD).

The Micromeritics Tristar II ASAP 3020 analyzer was used to conduct N_2 physisorption at 77 K. To remove any adsorbed contaminants and moisture on the surface, the samples were outgassed in a Micromeritics FlowPrep 060 under nitrogen. The iron-based oxides samples were outgassed at 200 °C for 2 h, while the samples containing zeolite were pretreated at 400 °C for 2 h. The specific surface area was determined according to the Brunauer-Emmett-Teller theory.

X-ray diffractograms of the powders were gathered at room temperature, using a Panalytical X'Pert Powder (Panalytical, Almelo, The Netherlands) diffractometer, with a PIXcel detector, operating at 40 kV and 40 mA, and employing a Ni β-filtered Cu-Kα radiation with a wavelength (λ) of $1.5406 \cdot 10^{-10}$ m. The XRD data were collected by scanning over the 2θ angle range of 5–80° using a step size of 0.013° 2θ and a time per step of 0.3 s. The average crystallite size of each phase was determined using Scherrer's equation. Moreover, to investigate in detail the evolution of the structure under reaction conditions, *in-operando* high temperature X-ray diffraction under reducing atmosphere is used. The samples were heated in a HTK1200N (Anton Paar, Austria), mounted on a Panalytical Empyrean (Panalytical, Almelo, The Netherlands) diffractometer with a PIXcel detector. More in detail, the *in-operando* tests were carried out on the fresh $NaFe_3O_4$_CP catalytic powder (≈160 mg) at different temperature by using a non-ambient program. The simulated reduction was performed by flowing 30 NmL·min^{-1} of 0.999 vol% H_2/Ar from 25 °C to 900 °C (heating rate: +10 °C·min^{-1}); the hold time prior the isothermal collection of the XRD pattern was 30 min. The simulated reaction was performed by pre-treating the sample with 30 NmL·min^{-1} of 0.999 vol% H_2/Ar at 450 °C for 15 h (XRD pattern were collected every 4 h). After the pre-treatment, the sample was cooled down to 330 °C and a gas mixture of 3 vol% H_2 and 0.5 vol% CO in N_2 (30 NmL·min^{-1}) was fed to the cell and XRD patterns were collected every 6 h at 330 °C under simulated reaction conditions. *In-operando* XRD data were collected from 20° to 80° of 2θ angle (scan per step: 0.013° 2θ, time per step: 0.60 s) using a high-resolution Bragg-Brentano detector.

The morphology of the catalysts was investigated by means of a field-emission scanning electron microscope (FE-SEM) Zeiss Merlin equipped with a Gemini-II column. Energy-dispersive X-ray spectroscopy (EDS) was also employed to identify the elemental composition of certain sections of the catalysts. In addition, transmission electron microscopy (TEM) images were registered by a FEI Tecnai F20ST operating at an accelerating voltage of 200 kV.

Sodium content in Fe-based catalyst and Si/Al ratio of the zeolite were measured by means of XRF, using a Wavelength Dispersive X-ray Fluorescence spectrometer (Rigaku Supermini 200) equipped with three standard crystals (LiF200, PET, and RX26).

X-ray photoelectron spectroscopy (XPS) was employed to analyze the surface of the catalyst using a PHI 5000 Versa Probe device. For survey scans, a band-pass energy of 187 eV, a 45° take-off angle, and a 100 μm X-ray spot diameter were used, whereas high-resolution (HR) spectra were obtained using a band-pass energy of 23 eV.

Temperature-programmed measurements were performed using Thermoquest TPD/R/O 1100 analyzer equipped with a thermal conductivity detector (TCD). The samples were initially subjected to H_2-TPR to investigate their reducibility properties. 15 mg of calcined sample were placed in a quartz tube reactor and pretreated at 400 °C for 1 h in Ar flow (30 mL·min^{-1}) to remove surface contaminants. Then, each sample was cooled down to 50 °C, and H_2-TPR measurements were carried out by heating the oven from 50 °C to 900 °C (with a ramp of 10 °C·min^{-1}) using a constant flow rate of 30 mL min^{-1} from a certified gas cylinder containing 5.0 vol % of H_2 in Ar.

Ammonia temperature-programmed desorption (NH_3-TPD) was performed on 50 mg of fresh and aged sample containing zeolite to determine the total acidity of the zeolite and core-shell structures. The sample was pretreated in situ with pure He (30 mL·min^{-1}) at 350 °C for 2 h. After pretreatment, the sample was cooled down to 50 °C and exposed to a 0.25 vol% NH_3/He flow (30 mL·min^{-1}) for 1 h at 50 °C. Following adsorption, the system was purged with He gas (30 mL·min^{-1}) for 30 min to remove physisorbed NH_3. Desorption was then carried out by heating the sample from 50° to 900°C at a rate of 10 °C min^{-1} under a He flow (30 mL·min^{-1}).

The study also includes an investigation of the interaction between CO_2 and the fresh/spent catalysts through CO_2-TPD measurements. Approximately 100 mg of the spent sample were placed between two layers of quartz wool in a quartz tube reactor and purged with He (30 mL·min^{-1}) at 350 °C (+10 °C·min^{-1}) for 2 h. The sample was then cooled down to 50 °C in He and saturated with 10.00 vol% CO_2/He (30 mL·min^{-1}) at 50 °C for 1 h. After saturation, the system was purged with He gas (30 mL·min^{-1}) for 30 min to remove physisorbed CO_2. Desorption was then performed by increasing the temperature from 50° to 900°C (+10 °C·min^{-1}) while flowing 30 mL·min^{-1} of He.

Lastly, the surface content of carbonaceous compounds on the spent catalysts was estimated by conducting temperature-programmed combustion (TPC) analyses. To perform the analysis, about 50 mg of each sample were placed in a U-shaped quartz tube, and a flow of 100 NmL·min^{-1} of 5 vol % O_2/N_2 was passed through the reactor from room temperature to 750 °C at a heating rate of + 10 °C·min^{-1}. The gas exiting the reactor was analyzed using an ABB Uras 14 gas analyzer to determine the concentrations of CO and CO_2.

2.3. Catalytic tests

Catalytic performance of the investigated samples was evaluated in a test bench equipped with a fixed-bed stainless steel reactor. The reactor has an inner diameter of 8 mm and there is an inner tube of 3.2 mm, containing a sliding thermocouple that allows to monitor the reaction temperature

profile within the catalytic bed, which is placed in the annular section of the reactor.

The catalyst load was set at 1.0 g for the iron-oxide phase and a total of 2.0 g when also the zeolite was present, in order to keep the spatial velocity (referred to the oxide phase) constant. The catalyst was firstly pretreated in situ under 50 vol% H_2/N_2 at a flow rate of 22 $NL \cdot h^{-1}$ and a pressure of 0.2 MPa. Time-on-stream (TOS) tests up to ~14 h were carried out at a temperature of 330 °C, a pressure of 2.3 MPa, and a flow rate of 22 $NL \cdot g_{Fe3O4}^{-1} \cdot h^{-1}$ with an inlet $H_2/CO_2/N_2$ molar ratio equal to 15/5/3.

The gaseous hydrocarbon products obtained during the tests were analyzed and quantified using an on-line gas chromatograph (7890B GC System, Agilent Technologies) equipped with a heated transfer line (120 °C, atmospheric pressure), a two-column separation system (HP-5 and HP-PLOT/Q) connected to a thermal conductivity detector (TCD) and a flame ionization detector (FID). An in-line gas analyzer (Emerson X-STREAM) equipped with two nondispersive infrared (NDIR) sensors and a thermal conductivity detector (TCD) monitored CO, CO_2, and H_2 molar fraction. The heavy hydrocarbon products, on the other hand, were condensed in a tank at room temperature and 2.3 MPa, and the collected oil was injected into a GC-MS for a qualitative analysis of the C_{6+} product obtained. Therefore, the selectivity for C_{6+} compounds was calculated as the complement to 100% with respect to the continuously analyzed gaseous products and the amount of oxygenated compounds. The aqueous fraction of collected liquid was analyzed via high performance liquid chromatography (HPLC) and total organic carbon (TOC) techniques in order to determine the selectivity to oxygenates. The experiment was designed to investigate the product evolution over time and to characterize the catalyst and products at the end of the test.

The amount of CO_2 that has been converted into products (ζ_{CO_2}), and the selectivity (σ_i) for the generic i-th product were calculated according to Eqs. (7) and (8), respectively:

$$\zeta_{CO_2} = \frac{\dot{n}_{CO_2,in} - \dot{n}_{CO_2,out}}{\dot{n}_{CO_2,in}} \tag{7}$$

$$\sigma_i = \frac{\dot{n}_{C,i,out}}{\dot{n}_{CO_2,conv}} = \frac{N_{C,i} \cdot \dot{n}_{i,out}}{\dot{n}_{CO_2,in} - \dot{n}_{CO_2,out}} \tag{8}$$

Where $\dot{n}_{CO_2,in}$ and $\dot{n}_{CO_2,out}$ are inlet and outlet dioxide carbon molar flow rate, respectively. $N_{c,i}$ represents the number of carbon atoms in a produced species, since selectivity is evaluated on carbon atoms balance instead of a stochiometric relation between reactants and products.

For each hydrocarbon class (j, grouping all molecules having the same number of carbon atoms, including isomers) the olefinic share for hydrocarbon classes between C_2 and C_4 has been defined and calculated as the ratio between olefins amount and the whole hydrocarbon production (i.e., paraffins plus olefins).

$$OS_j = \frac{\dot{n}_{j,O}}{\dot{n}_{j,O} + \dot{n}_{j,P}} \tag{9}$$

Concerning the FID response factor, the most significant light hydrocarbons (i.e., methane, ethylene, ethane, propylene, propane, 1-butylene, n-butane, 1-pentene and n-pentane) were calibrated with certified cylinders, whilst the response factor of the FID of other compounds was estimated according to the procedure proposed by Scanlon and Willis (Scanlon and Willis, 1985). The total outlet molar flow rate ($\dot{n}_{out}$) was estimated by assuming that the inert nitrogen molar flow rate did not vary during the process, as reported in Eq. (6); where $\dot{n}_{in}$ ($mol \cdot s^{-1}$) is the total inlet molar flow rate, $y_{N_2,in}$,in and $y_{N_2,out}$ are the inlet and outlet N_2 molar fraction, respectively.

$$\dot{n}_{out} = \dot{n}_{in} \cdot \frac{y_{N_2,out}}{y_{N_2,in}} \tag{10}$$

At the end of the catalytic tests, the catalyst was removed from the reactor and sieved to separate the spent sample from quartz wool fibers.

3. Result and discussion

3.1. Characterization of the catalysts

The results of the N_2 adsorption-desorption analysis carried out on all the samples can be found in Figs. S1, S2, and S3. All the fresh catalysts showed a type IV isotherm. However, there were some differences occurred in the observed hysteresis loop. The samples containing iron (Fig. S1) exhibited an H1-type hysteresis loop, indicating the formation of porous materials due to the agglomeration of uniformly sized spheres (Wei et al., 2016). Meanwhile, the zeolite samples (Fig. S2) exhibited a type IV isotherm with an H4-type hysteresis loop due to the presence of a significant number of slit-shaped pores, which were categorized as supermicropores and mesopores (Serrano et al., 2008; Wen et al., 2020). Thereby, Fig. 2 compares the pore distribution of the homemade hierarchical zeolite (HZ) and the commercial zeolite (HZSM5). HZ showed a wide distribution of pore sizes ranging from 50 Å to 200 Å, with a peak at around 90 Å, while the commercial zeolite had a narrower distribution. Table 1 provides chemical composition and textural properties of the investigated catalysts. XRF analysis for the two core-shell structures revealed an actual mass ratio of Na-Fe_3O_4_CP:zeolite of 1:1. As for the zeolites, the XRF analysis showed that the Si/Al atomic ratio was close to the nominal value for both commercial and hierarchical samples. In addition, hierarchical zeolite has a higher surface area (≈ 463.8 $m^2 \cdot g^{-1}$) than the commercial one (≈ 393.7 $m^2 \cdot g^{-1}$), a higher average pore size, and a greater total pore volume, confirming its mesoporous structure. Sodium content of the 1%$NaFe_3O_4$_WI and 5%$NaFe_3O_4$_WI samples was close to the nominal value, whilst $NaFe_3O_4$_CP sample obtained by

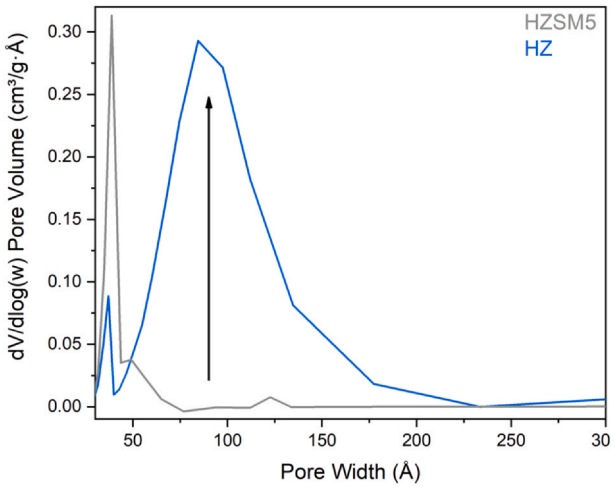

Fig. 2 – Pore size distribution.

Table 1 – Chemical composition and textural properties of fresh catalysts.

	Na/Fe_3O_4 (wt%)[a]	Si/Al[a]	$g_{NaFe3O4\_CP}$:g_{H-ZSM5} mass ratio[a]	BET surface area ($m^2 \cdot g^{-1}$)	Pore Volume ($cm^3 \cdot g^{-1}$)[b]	Pore size (Å)[c]
1%$NaFe_3O_4$_WI	1.3	-	-	50.1	0.28	199
5%$NaFe_3O_4$_WI	4.5	-	-	53.1	0.15	115
$NaFe_3O_4$_CP	4.7	-	-	87.2	0.27	94
HZSM5	-	38.0	-	393.7	0.11	38
HZ	-	39.5	-	463.8	0.29	102
$NaFe_3O_4$_CP@HZSM5	4.8	37.5	1:1	267.1	0.17	73
$NaFe_3O_4$_CP@HZ	4.7	39.6	1:1	371.4	0.28	77

[a] Calculated via XRF analysis
[b] BJH Desorption cumulative volume of pores between 17 Å and 3000 Å width
[c] BJH Desorption average pore width (4 V/A)

coprecipitation had a sodium content of 4.7 wt%. Interestingly, this sample exhibited the highest surface area (approximately 80 $m^2 \cdot g^{-1}$) while the surface area of the two samples obtained by impregnation was about 50 $m^2 \cdot g^{-1}$. This variation could be attributed to the different preparation methods, which may have caused the effective dispersion of sodium components on the Fe_3O_4 microspheres. In addition, the $NaFe_3O_4$_CP sample smaller pore size and larger surface area are likely due to the numerous inter-particle pores present within it. This, in turn, has the potential to significantly affect the mass transport rates of both the feed and FTS products (Cho et al., 2016). Finally, the surface area of the core-shell structures was also closely related to the Fe_3O_4-based and zeolite used; and, as expected, the XRF analyses confirmed that the $NaFe_3O_4$_CP:zeolite mass ratio was 1:1.

Fig. 3(a) displays the XRD patterns of the fresh Fe_3O_4-based catalysts. Samples 1%$NaFe_3O_4$_WI, 5%$NaFe_3O_4$_WI and $NaFe_3O_4$_CP exhibited the crystal planes (220), (331), (540), (511), and (440) of the typical magnetite Fe_3O_4 observed at 30.1°, 35.5°, 43.1°, 57.0°, and 62.6°, respectively. In the 5% $NaFe_3O_4$_WI sample, Na nitrate peak was detected, most likely due to the poor dispersion of Na on the surface of Fe_3O_4. Conversely, no diffraction peak associated with Na was observed in the other two samples, suggesting good dispersion of sodium, which seems to be affected by the different Na content and synthesis preparations, as seen in 1%$NaFe_3O_4$_WI and $NaFe_3O_4$_CP samples (Wen et al., 2020; Xu et al., 2019). On the other hand, Fig. 3(b) illustrates that the XRD patterns of the spent Fe_3O_4-based catalysts exhibited clear peaks of Fe_3O_4 and Fe_2C_5. According to the literature, these two phases are considered as responsible for the CO_2 conversion to CO and its subsequent hydrogenation to Fischer-Tropsch products, respectively (Wei et al., 2018, 2017). Scherrer's formula was used to determine the crystallite size of the fresh and spent Fe_3O_4 nanoparticles, based on the broadening of the most intense peak (311) at a 2θ angle value of 35.52° (Wei et al., 2016). The results of this calculation are provided in Table S1, showing that the coprecipitated $NaFe_3O_4$_CP sample has the smallest crystallite size, while the 1%$NaFe_3O_4$_WI sample has the largest crystallite size (11.4 nm and 17.8 nm, respectively). This trend also holds for the spent catalysts, whose size increases to 16.6 and 31.6 nm for impregnated and coprecipitated sample, respectively. The same growth trend from the fresh to the spent catalyst is noticeable for the 5%$NaFe_3O_4$_WI sample, whose values are close to those obtained for the $NaFe_3O_4$_CP sample.

Fig. 4(a) shows that homemade hierarchical zeolite (HZ), commercial zeolite (HZSM5), and the two core-shell structures ($NaFe_3O_4$_CP@HZSM5 and $NaFe_3O_4$_CP@HZ) exhibit diffraction peaks at 2θ values of 7.98°, 8.88°, 14.85°, 23.96°, and 24.38°, which are characteristic of the MFI topology structure (JCPSD No. 44–0002). Notably, the core-shell structures ($NaFe_3O_4$_CP@HZSM-5 and $NaFe_3O_4$_CP@HZ) show no evident peaks attributed to the iron phase. In fact, the peaks associated with the Fe_3O_4 phase are masked by the more intense zeolite peaks (this behavior also indicate that in both cases the zeolite is well dispersed on the surface of $NaFe_3O_4$_CP). Fig. 4(b), on the other hand, shows the XRD patterns of the spent catalysts, where the characteristic peaks of the MFI topology structure are present. However, it is

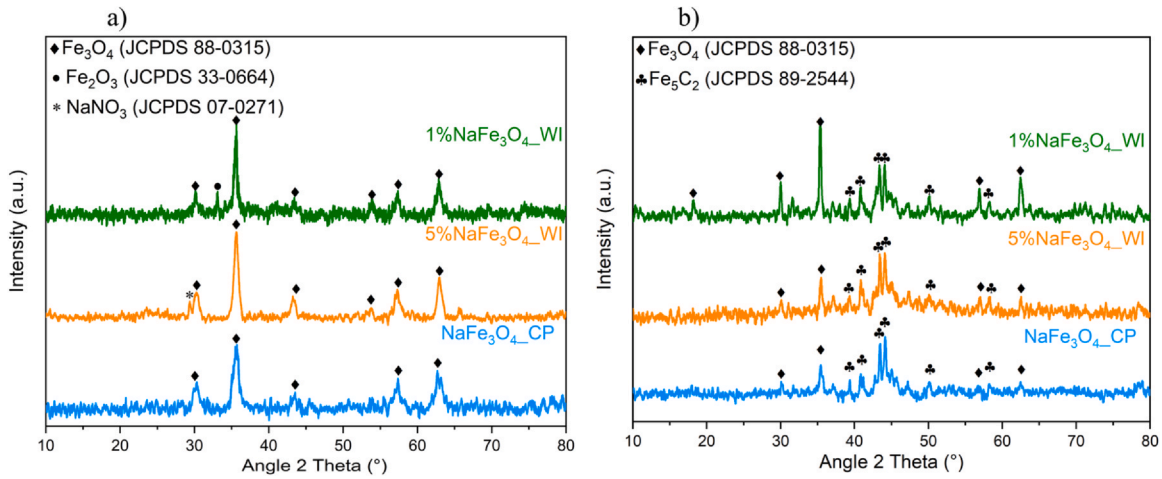

Fig. 3 – XRD patterns of the (a) fresh and (b) spent Fe_3O_4-based catalysts: 1%$NaFe_3O_4$_WI, 5%$NaFe_3O_4$_WI and Na-Fe_3O_4_CP.

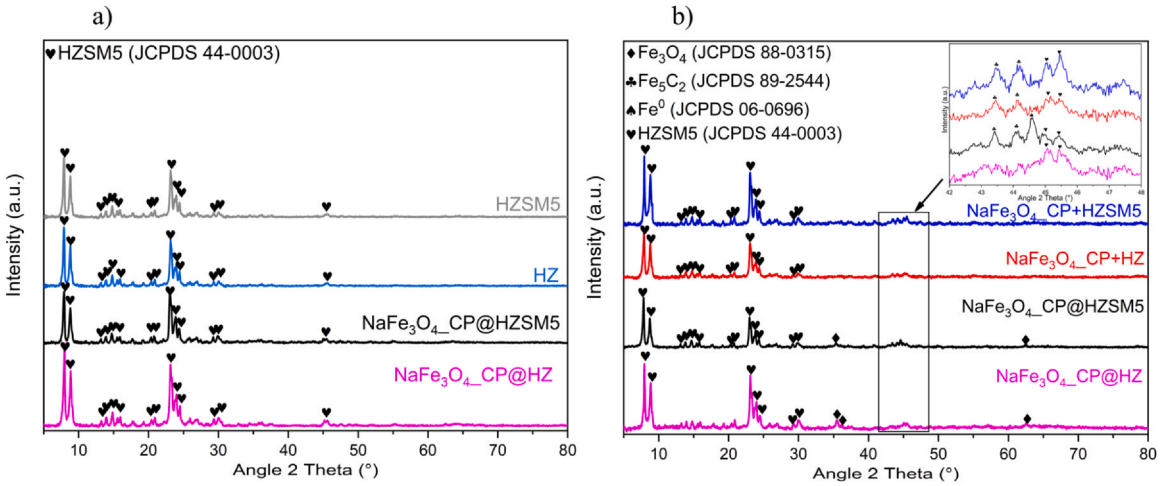

Fig. 4 – XRD patterns of (a) fresh zeolites and core-shell structures and (b) spent granule mixed catalysts and core-shell structures.

interesting to note the appearance of the peaks attributable to Fe_3O_4 (35.52°) and iron carbides (Fe_5C_2) at 42°–48° 2θ. In addition, the $NaFe_3O_4$_CP@HZSM5 sample deserves particular attention, as it is the only spent catalyst that exhibits a narrow and intense peak located at 44.6°; this peak has been attributed to the presence of metallic iron and could explain the lower activity of the catalyst during the modified Fischer-Tropsch reaction (see Section 3.2).

However, the presence of weak peaks related to iron carbide in Fig. 4(b) indicates that the higher crystallinity of the zeolite inhibits the intensity of the peaks related to iron phases. To effectively study the evolution of phases during the modified Fischer Tropsch, XRD in situ was performed on $NaFe_3O_4$_CP fresh catalyst. In particular, the patterns obtained by high temperature XRD for fresh Fe_3O_4-based catalyst under reducing atmosphere H_2/Ar are reported in Fig. S4. From room temperature to 400 °C only peaks related to Fe_3O_4 are present. At 450 °C the FeO and α-Fe phases appear, as shown by its characteristic peak at 2θ value of 41.6° and 44.6° respectively, while at 600 °C the Fe_3O_4 phase disappears. The patterns at 800 °C and 900 °C exhibit diffraction peak at 2θ value of 42.9° confirming the presence of the iron phase γ-Fe close to FeO and α-Fe. In Fig. 5(a) the patterns obtained by high temperature XRD under isothermal conditions at 450 °C for fresh $NaFe_3O_4$_CP catalyst under reducing atmosphere H_2/Ar are shown. The patterns collected every 4 h show the presence of Fe_3O_4, FeO and α-Fe, as well as their progressive growth over time. XRD patterns of fresh $NaFe_3O_4$_CP catalyst collected every 6 h at 330 °C under reducing atmosphere H_2/CO/N_2 and previously treated at 450 °C under reducing atmosphere H_2/Ar, are reported in Fig. 5(b). Distinct pattern of Fe_3O_4 and increasing over time peaks attributable to iron carbides (Fe_5C_2, Fe_7C_3) at 43°–46° 2θ are detectable (Bian et al., 2002; De Smit et al., 2010; Riedel et al., 2003; Zhang et al., 2022).

The presence of iron oxide phase in the fresh catalysts and iron carbide in spent ones was also investigated and evaluated measuring the interplanar distance of the crystal planes through HR-TEM analysis, as reported in Figs. S5 and S6. After the examination of the images, it becomes evident that the lattice spacing of the fresh nanoparticles, ranging from 4.6 to 5.3 Å, corresponds to the (111) face of Fe_3O_4. Conversely, the lattice spacing of the nanoparticles in the spent 1%$NaFe_3O_4$_WI catalyst is approximately 5.6 Å, which corresponds to the (200) face of Fe_5C_2. In the case of the spent $NaFe_3O_4$_CP catalyst, the lattice spacing of the nanoparticles is approximately 3.1 Å, corresponding to the (111) face of Fe_5C_2. Furthermore, the TEM image reported in Fig. S7 shows a particle from the spent sample of $NaFe_3O_4$_CP, where it is visibly evident that at the end of the catalytic test, the Fe_3O_4

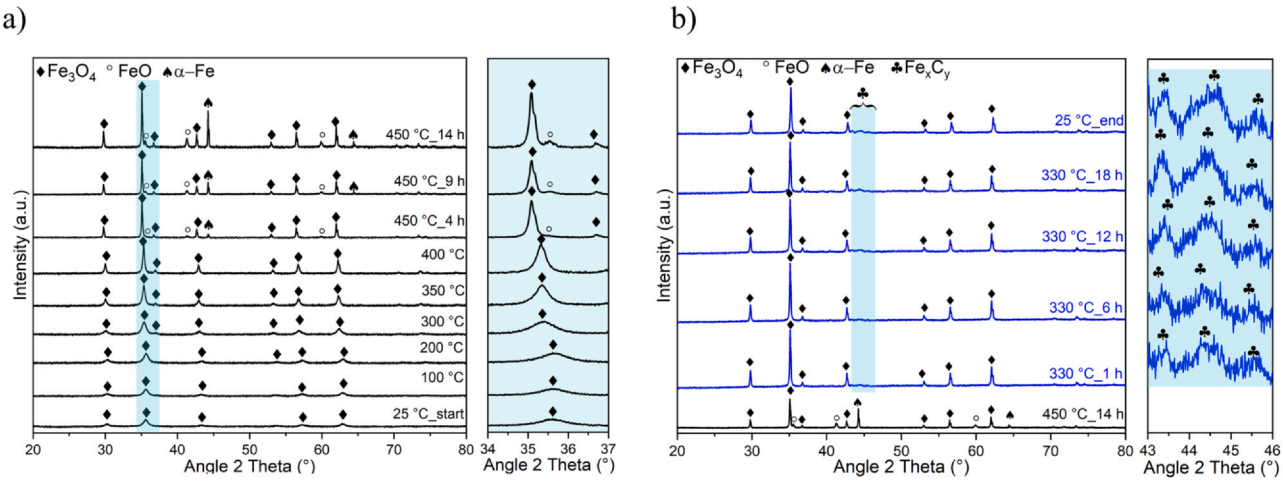

Fig. 5 – In situ XRD patterns of fresh $NaFe_3O_4$_CP catalytic powder under reducing atmosphere a) H_2/Ar from 25° to 450°C, black profiles; b) H_2/Ar at 450 °C for 14 h, black profile and $H_2/CO/N_2$ at 330 °C for 18 h, blue profiles.

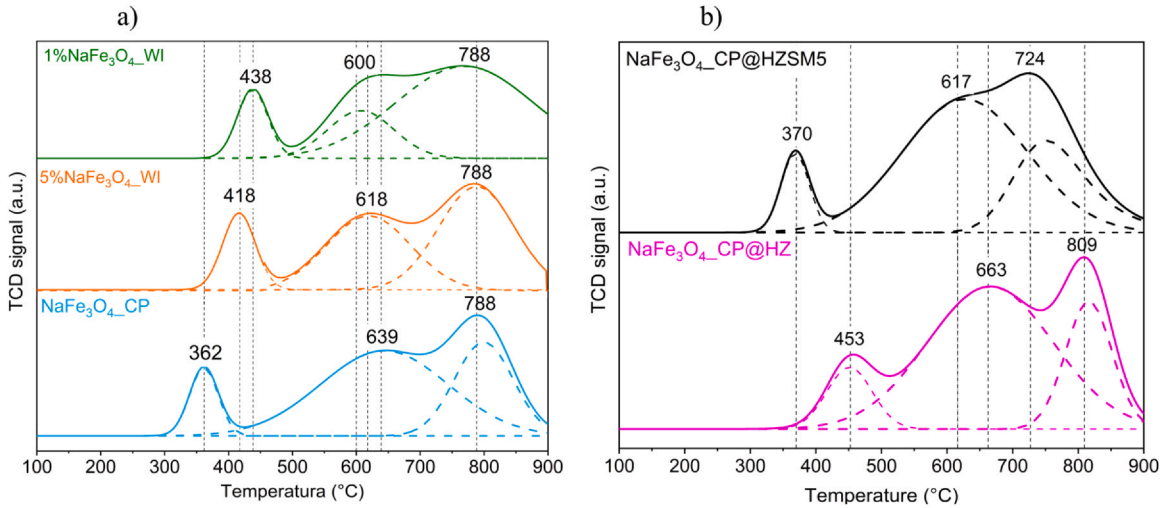

Fig. 6 – H_2-TPR profiles of fresh catalysts: (a) 1%Na-Fe_3O_4_WI, 5%Na-Fe_3O_4_WI 5%Na-Fe_3O_4_CP; (b) $NaFe_3O_4$_CP@HZSM5 and $NaFe_3O_4$_CP@HZ.

nanoparticles are surrounded by a layer of carbon, demonstrating how the catalyst undergoes modification during the catalytic test (Jin Chae et al., 2020; Panzone et al., 2020). On the other hand, TEM and SEM images for homemade HZ show that the sample is made by globular shape aggregates ranging from 200 to 400 nm and consisting of nanoparticles (Figs. S8 and S9). These nano-units form agglomerates containing ZSM5 nanocrystals, measuring 10–20 nm, with a similar morphology than the reference HZSM-5 sample (pictures not reported). The size of these aggregates is dependent on the chosen seed silanization agent, which in this case is 3-APTMS. The micrographs show the presence of additional porosity, which is created by the voids between the nanocrystals. The crystallographic planes of ZSM5 zeolite are visible throughout the particles, indicating a degree of orientation among adjacent nano-units and suggesting their likely intergrowth. This is remarkable considering the small size of the nano-units and confirms that these hierarchical MFI samples are highly crystalline materials (Serrano et al., 2008).

H_2-TPR profiles (Fig. 6) show the reduction behavior of iron-based catalysts with different Na content and distribution. In particular, Fig. 6(a) and (b) show that all catalysts exhibit three broad peaks centered in the range 362–438 °C, 600–639 °C, and 788 °C, and related to the reduction of Fe_2O_3 to Fe_3O_4, Fe_3O_4 to FeO, and FeO to metallic Fe, respectively (Abbaslou et al., 2009). Focusing on Fig. 6(a), the sample obtained by coprecipitation ($NaFe_3O_4$_CP) showed the lowest reduction temperature (362 °C), compared to the catalysts obtained by impregnation (1%$NaFe_3O_4$_WI and 5%Na-Fe_3O_4_WI), which exhibited the first reduction peak shifted to higher temperatures, at 438 and 418 °C, respectively. This result indicates that a different distribution and quantity of sodium would affect the reduction of Fe_2O_3 and Fe_3O_4. The results obtained from the deconvolution of the three peaks of H_2-TPR support this assumption and are reported in Table S2. It is worth highlighting that a higher sodium content, whether added directly by coprecipitation or subsequently by impregnation, does not significantly affect the H_2-uptake of the first peak, equal to 1.5, 1.6 and 1.8 mmol·g^{-1} for 1%Na-Fe_3O_4_WI, $NaFe_3O_4$_CP and 5%$NaFe_3O_4$_WI, respectively. This result is not surprising since, according to the XRD results (Fig. 3), there are no peaks clearly attributable to the Fe_2O_3 phase, except in the sample of 1%$NaFe_3O_4$_WI. Instead, the H_2-uptake of the second peak (Fe_3O_4 becoming FeO) is particularly low (2.0 mmol·g^{-1}) for the sample 1%$NaFe_3O_4$_WI if compared to 5%$NaFe_3O_4$_WI and $NaFe_3O_4$_CP where the H_2-uptake was 7.4 mmol·g^{-1} and 9.5 mmol·g^{-1}, respectively. Table S2 and Fig. 6(b) show that for the core-shell structure the peaks are shifted towards higher temperatures. Furthermore, the total H_2 consumption of the first two peaks is in both cases lower than the value obtained for the parent active phase alone. This aspect is even more evident in core-shell type structures, where the first reduction peak is shifted towards slightly higher temperatures compared to the parent active phase used ($NaFe_3O_4$_CP) as core. In fact, the first peak shifted to 370 °C for the sample $NaFe_3O_4$_CP@HZSM5 and 453 °C for $NaFe_3O_4$_CP@HZ catalyst, while the H_2-uptake decreased from 11.1 mmol·g^{-1} for the $NaFe_3O_4$_CP phase alone to 10.6 mmol·g^{-1} and 10.2 mmol·g^{-1} for the corresponding core-shell structures. A possible explanation deals with that the proximity between the iron phase and zeolite, that may influence the reducibility of the catalyst, and therefore its catalytic performance. This could also be related to the mass transfer phenomena of H_2 in the layer of zeolite that surround the oxide, which would delay the consumption of H_2 and thus lead to a shift to higher temperatures and/or Na migration.

To support Na migration and/or mass transfer phenomena assumption, NH_3-TPD tests were carried out to evaluate and compare the acidity of the core-shell structures with the parent zeolite used as shell, as shown in Fig. 7. The commercial zeolite (HZSM5) and the hierarchical one (HZ) exhibit a total acidity of 263 μmol·g^{-1} and 273 μmol·g^{-1}, respectively (Table S3); the concentration of acid sites within the hierarchical zeolite is comparable to that of the commercial zeolite, providing evidence that the synthesis was successful. The NH_3-TPD profiles of $NaFe_3O_4$_CP@HZSM5 and $NaFe_3O_4$_CP@HZ core-shell structures present a single, wider peak with a shoulder at a lower temperature of about 10–40 °C compared to the respective zeolite used as the shell. In addition, the peak at a higher temperature (350–400 °C) is completely absent. This result can be justified by the migration of sodium (promoter) from the mixed iron oxide phase towards the zeolite, since NaZSM-5 zeolite results in the absence of strong acid sites capable to adsorb NH_3

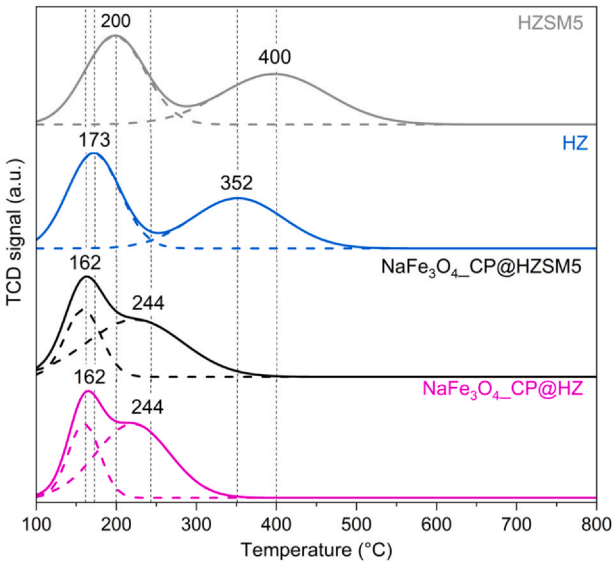

Fig. 7 – NH_3-TPD fresh catalysts profiles.

molecules, owing to the absence of a proton (H^+) linked to the O atom in the –Al–O–Si– group (Xu et al., 2020). On the other hand, the concentration of acid sites of fresh and spent sample is similar, indicating that the total amount of acid sites remains constant (Table S3).

The degree of coverage for the core-shell $NaFe_3O_4$_CP@HZSM5 was investigated via FESEM-EDS analysis, as reported in Fig. 8. The samples were prepared by cutting a section of sample with a scalpel and placing the hemisphere on the appropriate stub. The procedure was facilitated by the electrostatic properties of iron-phase located in the core, which allowed the pellet to be precisely positioned. As can be seen from Fig. 8, the sample was perfectly coated with zeolite.

Basic properties of fresh and spent catalysts were investigated by CO_2-TPD measurements. Fig. 9(a) and Fig. 10 (a) show the CO_2 desorption profiles for fresh iron-oxide phase catalysts and fresh core-shell $NaFe_3O_4$_CP@HZSM5, respectively. Figs. 9(b) and 10 (b) show the desorption profiles for the corresponding spent catalysts. The fresh catalysts exhibit a desorption peak at relatively low temperature, especially in the case of $NaFe_3O_4$_CP catalyst (156 °C), attributed to the desorption of weakly adsorbed CO_2. This peak is virtually absent in the 5%$NaFe_3O_4$_WI catalyst. Intense and broad peaks appear in the temperature range of 400–900 °C in the TPD profiles of the 1%$NaFe_3O_4$_WI and 5%$NaFe_3O_4$_WI catalysts. These peaks result from the desorption of CO_2 that strongly interacts with the surface basic sites. The presence of sodium is crucial in improving the surface basicity, as indicated by these results. The total CO_2 uptake amount of 5%$NaFe_3O_4$_WI shows that the surface basicity increases with increasing sodium content (Table 2). However, the surface basicity does not depend only on the amount of sodium, but also on its distribution on the catalyst surface (Wei et al., 2016). With the introduction of zeolite (core-shell structure $NaFe_3O_4$_CP@HZSM5), the first peak shifts towards a temperature about 100 degrees higher if compared with the core phase profile ($NaFe_3O_4$_CP). Focusing on the CO_2-TPD profiles of the spent catalysts (Figs. 9(b) and 10 (b)) there is at least one peak at a temperature above 520 °C. The absence of CO_2 desorption peaks below 400 °C indicates the absence of relatively weak basic sites on the surface of spent catalysts, implying that the weaker basic sites on the surface of fresh catalysts have become stronger compared to their spent counterparts (Yang et al., 2021). Moreover, the number of basic sites for all spent catalysts increases significantly after the CO_2 hydrogenation reaction (Table 2). It should also be noted that the higher the Na load in the catalyst, the greater

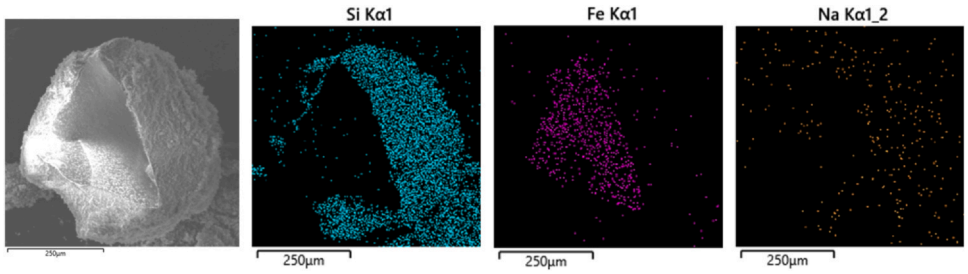

Fig. 8 – FESEM-EDS images of the sample: $NaFe_3O_4$_CP@HZSM5.

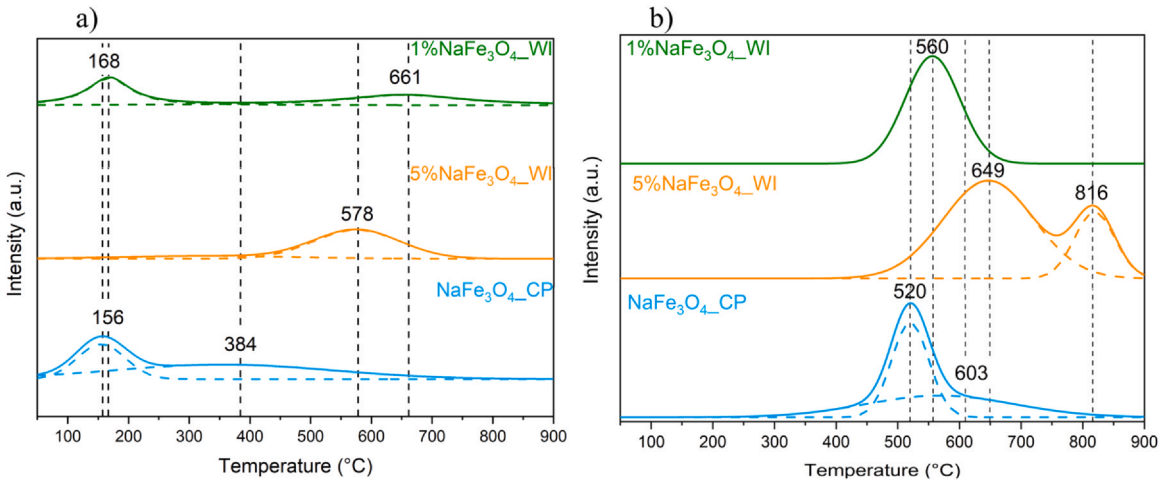

Fig. 9 – CO_2-TPD profiles a) fresh iron-oxide and b) spent iron-oxide samples.

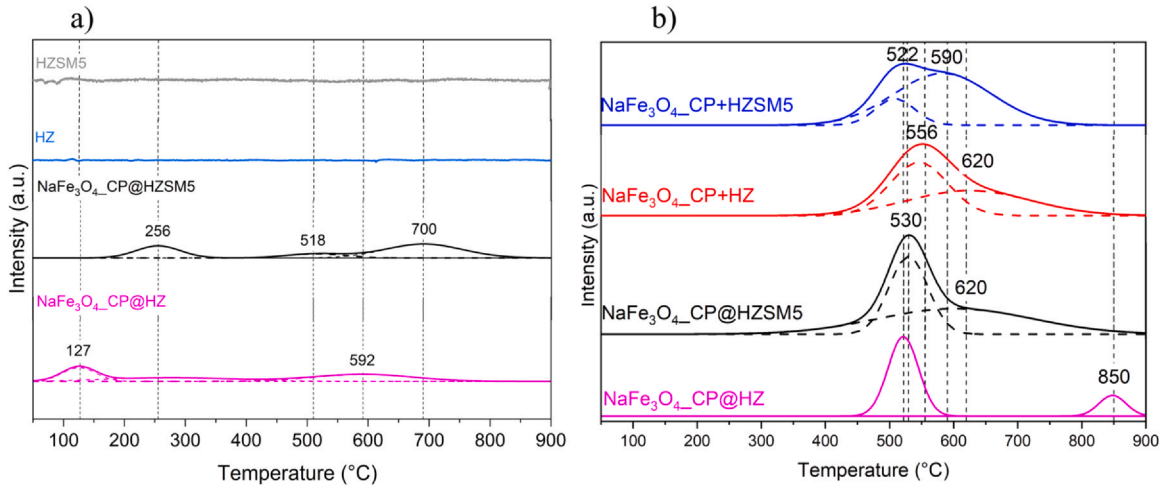

Fig. 10 – CO_2-TPD profiles a) fresh core-shell catalysts and their counterpart zeolite; b) spent core-shell structures and physical mixture.

Table 2 – CO_2-TPD fresh and spent iron-oxide phases.

	Fresh sample (mmol/$g_{iron\text{-}oxide\ phase}$)	Spent sample (mmol/$g_{iron\text{-}oxide\ phase}$)
1%$NaFe_3O_4$_WI	0.2	3.6
5%$NaFe_3O_4$_WI	0.7	3.9
$NaFe_3O_4$_CP	0.5	3.9
$NaFe_3O_4$_CP+HZSM5	-	3.7
$NaFe_3O_4$_CP+HZ	-	4.2
$NaFe_3O_4$@HZSM5	0.3	3.1
$NaFe_3O_4$@HZ	0.1	3.4

the amount of desorbed CO_2. Finally, comparing the amount of CO_2 per unit of mass of Fe_3O_4 of spent catalysts with and without a zeolite, it is possible to see that the amount of desorbed CO_2 decreases significantly in the core-shell $NaFe_3O_4$_CP@HZSM5 structure (Table 2). This could imply that the presence of zeolite in intimate contact with the $NaFe_3O_4$_CP phase negatively affects the adsorption of CO_2.

To better understand where Na was located and if the core-structures were well covered by the zeolite, XPS measurements have been performed on the following samples (both fresh and spent): 1%$NaFe_3O_4$_WI, 5%$NaFe_3O_4$_WI, $NaFe_3O_4$_CP, $NaFe_3O_4$_CP@HZSM5 and $NaFe_3O_4$_CP@HZ. In particular, survey scans have been recorded firstly, to infer the presence of chemical elements and to calculate their relative atomic concentration (at%); scans are reported in Fig. S10. The chemical composition obtained for each sample is resumed in Table 3. According to the literature (Chai et al., 2022) we expected a decrease in the Fe concentration after the catalytic tests, due to the formation of a passivation layer made principally by carbon species. This trend is clearly noticeable for samples 1%$NaFe_3O_4$_WI, 5%$NaFe_3O_4$_WI and $NaFe_3O_4$_CP, while the core-shell structures did not show a clear trend, as iron oxide is cover by zeolite shell. Carbon content for sample $NaFe_3O_4$_CP@HZSM5 can be considered mostly stable, while for sample $NaFe_3O_4$_CP@HZ the carbon content decreases after catalytic tests. Fe signal appeared after catalytic tests in both zeolite covered samples, with very low intensity (≤ 1.0 at %), maybe due to shell erosion or fractures, which make Fe_3O_4 core exposed. Na1s signal has a not clear trend as well: it increases for wet impregnated samples, after catalytic tests, while decreases for co-precipitated one; it is almost constant for core-shell structures (according to Fe content). Some remnants due to precursors have also been detected (i.e., Cl and S). It should be underlined that only for sample 5%$NaFe_3O_4$_WI_f a N1s peak has been detected. From subsequent HR analysis (see Fig. S10), we found out that the chemical shift inferred is the one related to $NaNO_3$ (407.4 eV) (C.D. Wagner et al., 2003), as already explained with XRD measurement. This contribution disappeared after catalytic tests.

Focusing on the HR spectra acquired for all the elements, which are crucial to understand the behavior of catalysts surfaces, we can appreciate several modifications due to catalytic tests. In Fig. 11 (a, d) Fe2p spectra are reported, for

Table 3 – XPS relative atomic concentration (at%) for all the samples, fresh and spent ones.

SAMPLES	Relative atomic concentration (at%)						
	C1s	O1s	Fe2p	Na1s	Si2p	Others	
1%$NaFe_3O_4$_WI	10.9	67.3	14.6	2.3	/	Cl: 0.5; S: 4.4	fresh
	37.1	46.9	3.9	4.8	/	Cl: 0.3; S: 7.0	spent
5%$NaFe_3O_4$_WI	19.9	48.8	21.1	7.8	/	N: 2.4	fresh
	61.9	23.7	3.2	11.2	/	/	spent
$NaFe_3O_4$_CP	11.4	53.5	9.6	14.2	/	Cl: 1.6; S: 9.7	fresh
	76.6	19.4	0.8	1.5	/	S: 1.7	spent
$NaFe_3O_4$_CP+HZSM5	18.2	61.3	/	/	20.5	/	fresh
	20.0	57.2	1.0	0.8	21.0	/	spent
$NaFe_3O_4$_CP+HZ	47.1	41.4	/	/	11.5	/	fresh
	9.3	60.3	0.4	1.1	28.0	Al: 0.9	spent

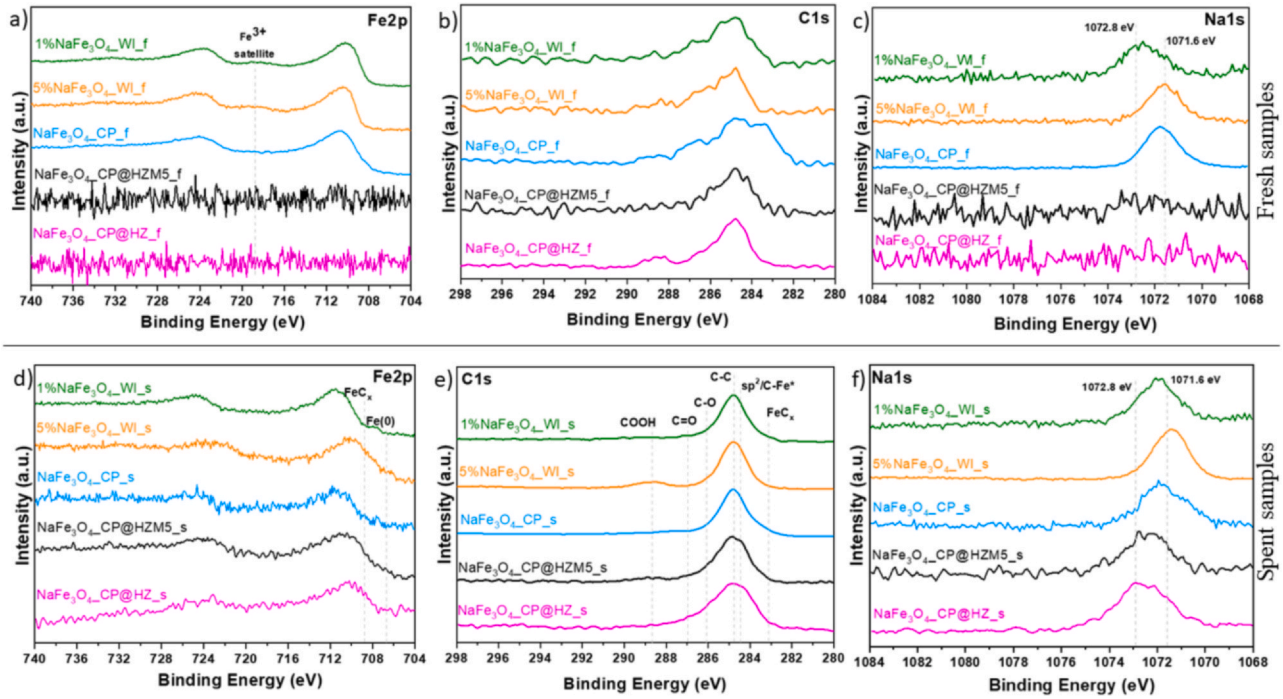

Fig. 11 – XPS HR spectra: Fe2p doublet (a, d), C1s region (b, e) and Na1s region (c, f) for fresh (upper row) and spent (lower row) samples.

both fresh and spent samples: the shape of curves for the WI fresh samples is the one reported for Fe_3O_4 (Grosvenor et al., 2004), with the typical satellite due to Fe^{3+} species at ≈ 719 eV. The $Fe2p_{3/2}$ peak position is at 710.3 eV (± 0.1 eV), as expected. For sample $NaFe_3O_4$_CP_f, the peak appears less sharp towards the lower binding energy, with an enlargement of the FWHM, due to the increase of the Fe^{2+} component (at 709.0 eV), which is furthermore evidenced by the quasi-disappearance of the satellite at 719 eV, which is due to Fe^{3+}. After the catalytic tests new components arise, in accordance with XRD results. In particular two components have been detected: a first one at 706.7 eV due to Fe(0) and a second one at 708.7 eV due to FeC_x (Guo et al., 2018). Both components are more intense in samples 5%$NaFe_3O_4$_WI_a and in the core-shell ones. In accordance to Fe2p changes also C1s peaks show different chemical shifts after the catalytic activity. Before tests, the C signal are quite noisy, due to the low intensity of the signals. After the tests the signals are sharper and deconvolution procedures (not shown) could be applied to them. Apart from the C-C due to adventitious carbon at 284.8 eV, several peaks due to C-O interaction are present at higher binding energy values, as reported in Fig. 11 (b, e). Only sample 5%$NaFe_3O_4$_WI_a shows a component at 288.6 eV, due to COOH species. If we look at the lower binding energies side, we can infer the appearance of two components: one due to FeC_x bond at 283.1 eV and another one at 284.5 eV, which can be due to C-C sp^2 arrangement or to C-Fe* charge transfer effects (Furlan et al., 2015) which appears when charge is transferred from the metal surface atoms to the more electronegative carbon atoms in the a-C matrix, which, in our case, can be represented by the outer C amorphous shell, as shown in TEM analysis previously. The last region we have analyzed is the one related to Na1s peak, Fig. 11 (c, f). Two main chemical shifts have been evidenced: a first one at lower binding energies at 1071.6 (± 0.2) eV and a second one at higher binding energies at 1072.8 (± 0.2) eV. According to the literature, it is possible to evaluate the possible migration of sodium from the Na1s signal. In fact, the position of Na1s signal has to be at 1071.4 eV, whereas the core-shell structures, after the heat treatment, showed a shift of the Na1s signal to 1073.0 eV, which is in the range of the sodium ion exchanged zeolite (1072.8 eV). This shift towards higher binding energy after the heat treatment supports the hypothesis of migration of sodium ions from the iron catalyst to the zeolite, resulting in loss of promotion effect on the iron catalyst as well as decreased acidity of the zeolite (Weber et al., 2020).

3.2. *Catalytic tests*

This section presents the outcomes of the catalytic experiments performed on iron-oxide phases synthesized through different techniques and with varying sodium content. Stability tests were carried out at 330 °C, a pressure of 2.3 MPa, and a flow rate of 21.96 NL·g_{Fe3O4}·h^{-1} with an inlet composition of 65 vol% H_2, 22 vol% CO_2, and 13 vol% N_2 over about 14 h.

As reported in the synthesis section, the samples named 1%$NaFe_3O_4$_WI, 5%$NaFe_3O_4$, and $NaFe_3O_4$_CP were obtained using two different synthesis methods (impregnation for 1% $NaFe_3O_4$_WI and 5%$NaFe_3O_4$ and coprecipitation for $NaFe_3O_4$_CP) and varying the sodium content from 1 wt% (g_{Na}/g_{Fe3O4}) in 1%$NaFe_3O_4$_WI, to 5 wt% (g_{Na}/g_{Fe3O4}) in 5% $NaFe_3O_4$_WI sample. To simplify the discussion of the catalytic tests, the results reflects the gas analysis outcomes at 11 h of testing (Fig. 14), while the TOS monitoring profiles are shown in Fig. S11 (a), (b), and (c). As can be seen from Fig. 14, the catalytic performance increases with increasing sodium content. CO_2 conversion passes from 22% in the 1%$NaFe_3O_4$_WI sample to 36–38% in the 5%$NaFe_3O_4$_WI and $NaFe_3O_4$_CP samples, demonstrating that the amount of loaded Na (rather than the synthesis method) seems to affect the catalytic performance (Wei et al., 2016). On the other hand, although the CO selectivity is approximately the same

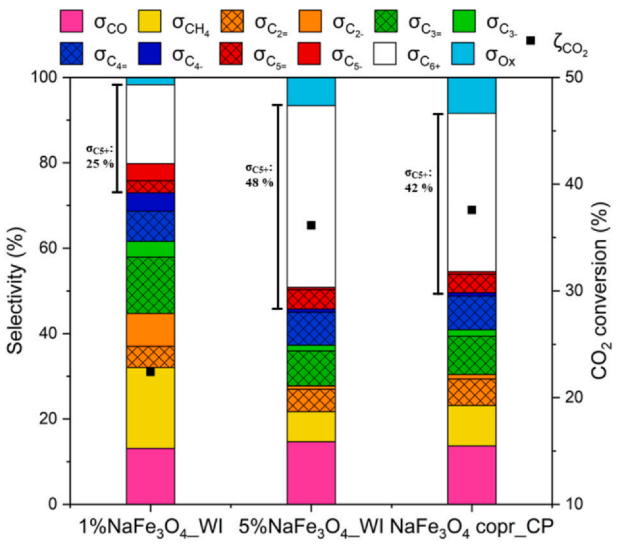

Fig. 12 – Comparison catalytic performance of 1% $NaFe_3O_4$_WI, 5%$NaFe_3O_4$_WI and $NaFe_3O_4$_CP catalysts at 330 °C. Reaction conditions: 2.0 MPa, 21.96 NL·gFe_3O_4·h^{-1}, TOS = 14 h.

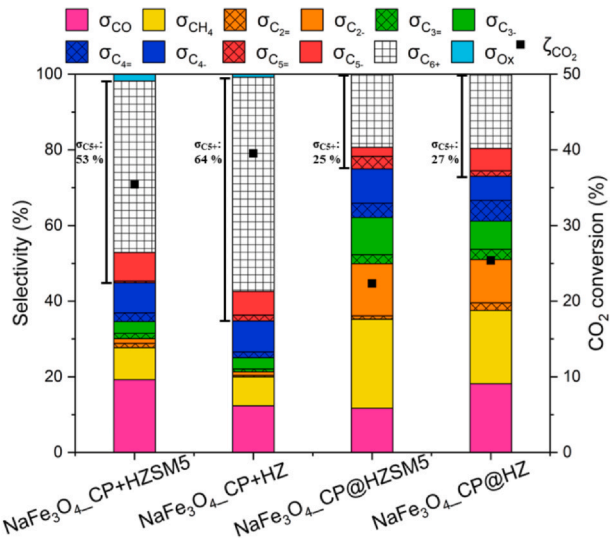

Fig. 13 – Comparison of catalytic performance among physical mixture and core-shell of $NaFe_3O_4$_CP with commercial and homemade hierarchical zeolite. Reaction conditions: 330 °C, 2.3 MPa, and a flow rate of 21.96 NL·g_{Fe3O4}·h^{-1} TOS= 14 h.

(ranging from 13% to 15% in all three samples), the methane selectivity is suppressed with increasing sodium content, in agreement with the open literature (Li et al., 2014). The CH_4 selectivity decreased from 19% (1%$NaFe_3O_4$_WI) to 7–9% for the other two catalysts. Furthermore, it is worth noting that as the sodium content increases, C_2-C_4 olefins selectivity increased significantly, reaching 88–87% for 5%$NaFe_3O_4$_WI and $NaFe_3O_4$_CP samples, respectively (Table S4). GC-MS chromatogram obtained by injecting the collected oil produced with $NaFe_3O_4$_CP sample is shown in Fig. S12, where the prevalence of olefinic compounds can be appreciated. Another interesting aspect is the selectivity of oxygenated compounds present in the collected aqueous fraction during condensation, calculated by considering the amount of cleaning solvent (acetone) used to clean the reactor and the lines of the test bench. Specifically, the amount of acetone resulting from HPLC analysis was subtracted from the mg·L^{-1} of carbon obtained through TOC analysis (Table S5), divided for the hours of TOS and subtracted as a complement to 100 with respect to the gaseous products analyzed continuously using GC-FID (Table S4 and Fig. 14). It is interesting to note that, although 5%$NaFe_3O_4$_WI and $NaFe_3O_4$_CP samples were obtained using different syntheses, the catalytic results obtained with the same sodium content are very similar, regardless of the preparation method (Wei et al., 2016). For simplicity of preparation, only the $NaFe_3O_4$_CP sample was tested in physical mixture mode and in core-shell structures with two different MFI-type zeolites (commercialHZSM5 and the homemade hierarchical HZ).(Fig. 12).

The interest in combining the iron-based catalyst with zeolite lies in the desire to obtain a liquid fuel with aromatic compounds, giving desirable properties to the final product, such as high octane number and improved engine combustion efficiency. Additionally, aromatic compounds are important for cleaner combustion because they have a higher tendency to burn completely than other gasoline components, thus reducing emissions of polluting exhaust gases. On the other hand, excessive amounts of aromatics can increase particulate emissions, so their presence in gasoline must be carefully controlled. To control the content of aromatic compounds, it is important to use zeolites with an appropriate Si/Al atomic ratio. In this work, zeolites with a Si/Al atomic ratio of 40 were chosen according to the open literature data. The experimental results for the samples containing both the metallic phase and a zeolite are reported in Fig. 13. $NaFe_3O_4$_CP catalyst tested in physical mixture with both the commercial and homemade hierarchical zeolites showed higher catalytic activity than the corresponding core-shell samples having the same active phase and zeolite. Specifically, the catalyst labelled as $NaFe_3O_4$_CP+HZ (physical mixture) turned out to have the best catalytic performance. This catalyst achieved a conversion of 40%, (compared to 35% obtained with $NaFe_3O_4$_CP+HZSM5 catalyst), a CO selectivity of 12% (compared to 19% by testing $NaFe_3O_4$_CP+HZSM5), and an 8% CH_4 selectivity. C_{6+} selectivity was 57% for $NaFe_3O_4$_CP +HZ, higher than the value (45%) obtained with $NaFe_3O_4$_CP +HZSM5 catalyst. Furthermore, for the most performing catalyst ($NaFe_3O_4$_CP+HZ) light olefins (C_2-C_4) selectivity and olefin share are the lowest among the investigated samples, being equal to 3% and 18%, respectively (Table S4). Limited olefins content and increased paraffins production, along with the formation of C_{6+} compounds, is a clear demonstration of the zeolite ability to oligomerize, isomerize, and aromatize how discussed in the introduction section.

Another interesting aspect is that the content of oxygenated compounds decreased when an acid zeolite is present within the catalyst (decreasing from 8% for the $NaFe_3O_4$_CP phase alone to below 2% in presence of a zeolite). Indeed, oxygenated compounds can be transformed directly into olefins and/or hydrogenated to paraffins. The superior catalytic performance of the hierarchical zeolite can be attributed to the presence of mesopores, which facilitate the desorption of aromatic and/or long-chain products due to the larger pore size. As can be appreciated from the chromatograms of the oil collected at the end of the 14-hour test and reported in Figs. S13 and S14, the majority of the compounds present in the C_{6+} fraction are aromatic compounds, both when using a commercial or a hierarchical homemade zeolite. This result

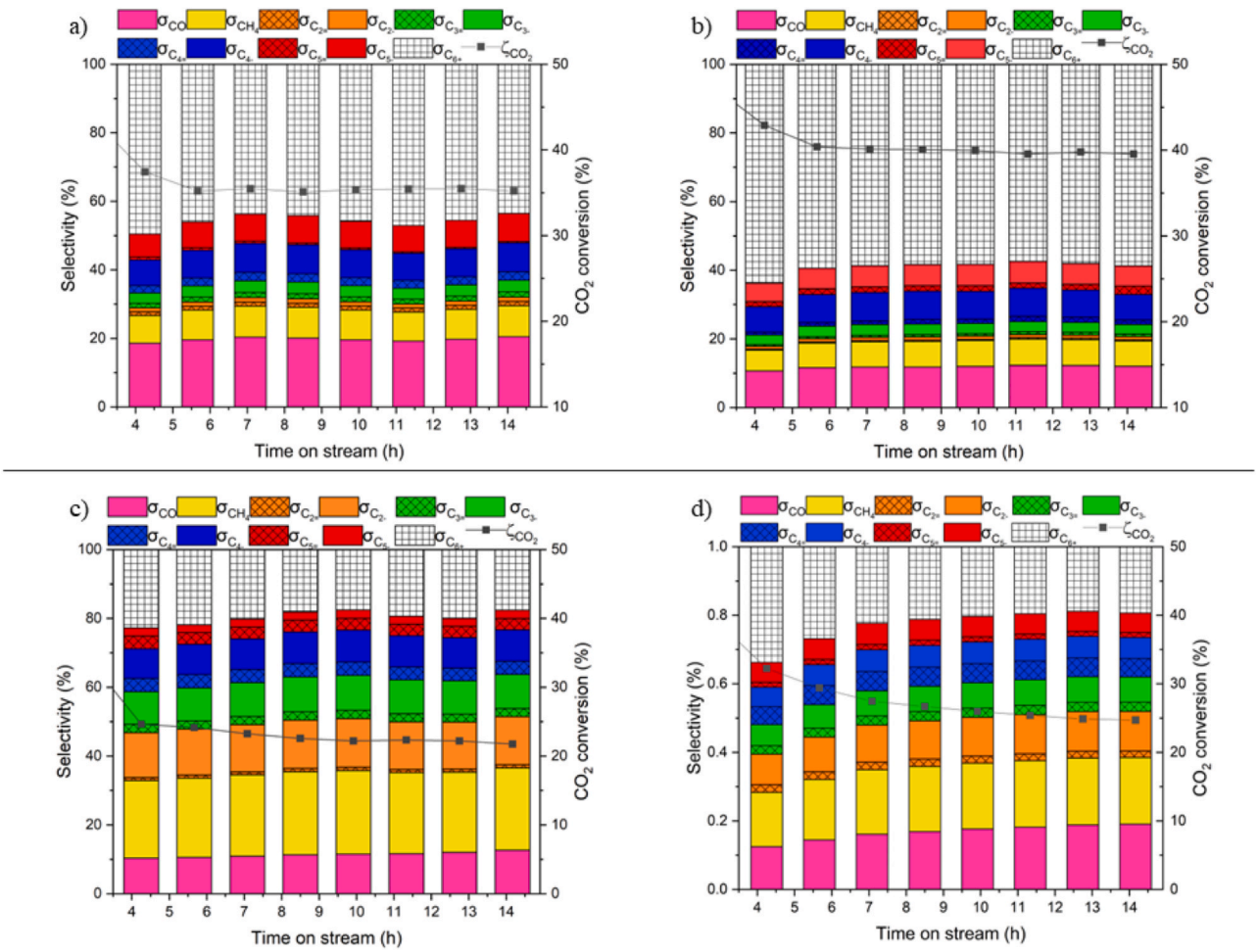

Fig. 14 – Time-on-stream (TOS) tests up to ≈ 14 h, temperature: 330 °C, pressure: 2.3 MPa, and flow rate: 22 NL·g^{-1}_{Fe3O4}·h^{-1} with an inlet $H_2/CO_2/N_2$ molar ratio equal to 15/5/3: a) $NaFe_3O_4$_CP+HZSM5; b) $NaFe_3O_4$_CP+HZ; c) $NaFe_3O_4$_ CP@HZSM5; d) $NaFe_3O_4$_CP@HZ.

demonstrates how the olefins produced on the active sites of the iron-based catalyst were converted into predominantly aromatic compounds on the acid sites of the zeolite, justifying the significant increase in selectivity towards C_{6+} compounds when the zeolite is involved. By referring to the TOC results, the hierarchical zeolite represents the one with lower content of oxygenated compounds (Table S5). Focusing on the core-shell configurations (Fig. 13), the idea was to achieve a layered structure able to minimize the diffusional path between the FTS sites where linear hydrocarbon products are obtained and the ones of the zeolite, where they are rearranged. Simultaneously, due to the generation of water during the FTS process and the need for rapid counter-diffusion to prevent limiting the CO_2 reaction, it was decided to investigate the effects of both a conventional zeolite (HZSM5) and a hierarchical zeolite (HZ). Looking to the results it is clear that the catalytic activity towards modified Fischer-Tropsch Synthesis (FTS) is lower than the one obtained with the corresponding physical mixtures and the iron-based catalyst alone (as indicated in Table S4). For instance, $NaFe_3O_4$_CP@HZSM5 catalyst exhibited a 13% lower conversion rate than the corresponding $NaFe_3O_4$_CP+HZSM5 that, how anticipated in the Section 3.1, could be correlated to the presents of metallic iron. In addition a decrease in conversion is also observed when comparing $NaFe_3O_4$_CP@HZ with $NaFe_3O_4$_CP+HZ. In order to elucidate the reduced performance of the two core-shell structures compared to their corresponding physical mixtures, careful examination of the TOS (Time-on-Stream) monitoring is necessary. This can be observed in Fig. 14 (a, b, c, d), where tests carried out using physical mixtures with a 1:1 mass ratio ($NaFe_3O_4$_CP:zeolite) demonstrated minimal changes over time. However, both core-shell structures exhibited a significant conversion decrease over time, as well as an increase in CO and CH_4 selectivity and a drop in C_{6+} selectivity. These observed trends, supported by the results obtained from XPS, NH_3-TPD, and H_2-TPR characterizations, can be ascribed to the migration of sodium from the $NaFe_3O_4$_CP phase to the zeolite, resulting in the transformation of the zeolite from its protonic H^+ form to its Na^+ form (Karre et al., 2012). Previous research suggested that a small distance between the iron (-carbide) catalyst and the acidic sites of a bifunctional catalytic system may facilitate the migration of alkali metal ions from the iron (-carbide) catalyst to the zeolite, owing to the high mobility of these ions. This may lead not only to decreased activity and selectivity of the catalyst, but also to neutralization of the zeolite acidic sites, resulting in lower olefin aromatization (Karre et al., 2012).

To rule out the deactivation of core-shell structures due to coke deposition, all spent catalysts were subjected to temperature programmed combustion (TPC) analysis to quantify the amount of carbon deposited on the surface of the samples during catalytic tests. Table 4 reports the quantity of carbon moles in the spent catalyst (generated during TPC

Table 4 – TPC results.

	g_{coke}/g_{cat} (a.u.)	mol $C_{spent\ catalyst}$/mol $C_{converted}$ (%)
1%$NaFe_3O_4$_WI	0.05	0.63
5%$NaFe_3O_4$_WI	0.15	1.16
5%$NaFe_3O_4$_CP	0.11	0.82
$NaFe_3O_4$_CP+HZSM5	0.07	0.60
$NaFe_3O_4$_CP+HZ	0.07	0.47
$NaFe_3O_4$_CP@HZSM5	0.02	0.25
$NaFe_3O_4$_CP@HZ	0.02	0.21

analysis) expressed as a percentage of the whole converted carbon over the entire time-on-stream investigation. The amount of coke deposit in the carbon is lower when the hierarchical zeolite is involved, confirming the importance of mesopore in the structure of the zeolite. In addition, based on the results of coke deposition, the core-shell structures lower activity is not due to deposited coke. In fact, the resulting coke is lower if compared to the catalysts that showed higher catalytic activity. The results emphasize that the core-shell structures are probably affected by diffusion problems and/or sodium migration issues. Moreover, it is possible that these two effects are interconnected, and investigating the underlying reasons for the limited activity of these structures presents an intriguing research opportunity.

4. Conclusion

The synthesis of stable and high-performing multifunctional catalysts for hydrocarbon mixture production via CO_2 hydrogenation (i.e., modified Fischer-Tropsch process) was investigated. Based on the results obtained, no significant differences were noticed between iron-based catalysts with the same sodium content obtained through impregnation and coprecipitation. Thus, in terms of energy saving, the use of the iron-based catalyst obtained through coprecipitation represents a valid alternative, since it can be synthesized in a single step (without pre-calcination before use) and requires a smaller amount of water. Physical mixture between Na-promoted Fe-based metallic phase and acid zeolites led to the best performance in terms of conversion and heavier hydrocarbons selectivity (mainly due to oligomerization and aromatization). Furthermore, it is evident that the use of a hierarchical zeolite is a valid alternative to increase the amount of products within the gasoline range. With the presence of mesopores that facilitate the release of products, the isomerization capacity is higher if compared to a conventional zeolite. As a future perspective, it will also be interesting to carry out in situ and/or post-reaction characterizations to study, confirm, and/or refute the migration of alkali metals, partly supported by the ex-situ XPS and NH_3-TPD analyses reported in this article. Alternatively, it will be necessary to study a support (possibly hydrophobic, such as carbon-based supports) preventing the migration of sodium and that help design a valid and high-performance core-shell catalyst.

Declaration of Competing Interest

The authors declare that they have no known competing financial interests or personal relationships that could have appeared to influence the work reported in this paper.

Acknowledgements

The authors would like to acknowledge the project PON Ricerca e Innovazione “REACT-EU” (DM 1062/21) funded by the Italian Ministero dell’Università e della Ricerca (MUR).

Appendix A. Supporting information

Supplementary data associated with this article can be found in the online version at doi:10.1016/j.cherd.2023.07.052.

References

Abbaslou, R.M.M., Tavassoli, A., Soltan, J., Dalai, A.K., 2009. Iron catalysts supported on carbon nanotubes for Fischer-Tropsch synthesis: Effect of catalytic site position. Appl. Catal. A Gen. 367, 47–52. https://doi.org/10.1016/j.apcata.2009.07.025

Bian, G., Oonuki, A., Koizumi, N., Nomoto, H., Yamada, M., 2002. Studies with a precipitated iron Fischer-Tropsch catalyst reduced by H_2 or CO. J. Mol. Catal. A Chem. 186, 203–213.

C.D. Wagner et al., 2003, NIST X-ray Photoelectron Spectroscopy (XPS) Database 20, Version 3.4 [WWW Document]. web version. URL https://srdata.nist.gov/xps/ (accessed 5.27.23).

Chai, J., Pestman, R., Chiang, F.-K., Men, Z., Wang, P., Hensen, E.J.M., 2022. Influence of carbon deposits on Fe-carbide for the Fischer-Tropsch reaction. J. Catal. 416, 289–300. https://doi.org/10.1016/j.jcat.2022.11.002

Cho, J.M., Jeong, M.H., Bae, W, Jong, 2016. Fischer-Tropsch synthesis on potassium-modified Fe_3O_4 nanoparticles. Res. Chem. Intermed. 42, 335–350. https://doi.org/10.1007/s11164-015-2360-3

Cui, X., Gao, P., Li, S., Yang, C., Liu, Z., Wang, H., Zhong, L., Sun, Y., 2019. Selective Production of Aromatics Directly from Carbon Dioxide Hydrogenation. ACS Catal. 9, 3866–3876. https://doi.org/10.1021/acscatal.9b00640

De Klerk, A., 2014. Transport fuel: biomass-, coal-, gas- and waste-to-liquids processes. Future Energy.: Improv., Sustain. Clean. Options our Planet 245–270. https://doi.org/10.1016/B978-0-08-099424-6.00012-0

De Smit, E., Cinquini, F., Beale, A.M., Safonova, O.V., Van Beek, W., Sautet, P., Weckhuysen, B.M., 2010. Stability and reactivity of ε-X-θ iron carbide catalyst phases in fischer-tropsch synthesis: Controlling μc. J. Am. Chem. Soc. 132, 14928–14941. https://doi.org/10.1021/JA105853Q/SUPPL_FILE/JA105853Q_SI_001.PDF

Dieterich, V., Buttler, A., Hanel, A., Spliethoff, H., Fendt, S., 2020. Power-to-liquid via synthesis of methanol, DME or Fischer–Tropsch-fuels: a review. Energy Environ. Sci. 13, 3207–3252. https://doi.org/10.1039/d0ee01187h

Energy Agency, I., 2021, Global Energy Review: CO_2 Emissions in 2021 Global emissions rebound sharply to highest ever level.

Fuhse, J., Bandermann, F., 1987. Conversion of organic oxygen compounds and their mixtures on H-ZSM-5. Chem. Eng. Technol. 10, 323–329. https://doi.org/10.1002/CEAT.270100139

Furlan, A., Jansson, U., Lu, J., Hultman, L., Magnuson, M., 2015. Structure and bonding in amorphous iron carbide thin films. J. Phys.: Condens. Matter 27, 045002. https://doi.org/10.1088/0953-8984/27/4/045002

Gambo, Y., Adamu, S., Lucky, R.A., Ba-Shammakh, M.S., Hossain, M.M., 2022. Tandem catalysis: A sustainable alternative for direct hydrogenation of CO_2 to light olefins. Appl. Catal. A Gen. 641, 118658. https://doi.org/10.1016/J.APCATA.2022.118658

Gao, P., Dang, S., Li, S., Bu, X., Liu, Z., Qiu, M., Yang, C., Wang, H., Zhong, L., Han, Y., Liu, Q., Wei, W., Sun, Y., 2018. Direct Production of Lower Olefins from CO_2 Conversion via Bifunctional Catalysis. ACS Catal. 8, 571–578. https://doi.org/10.1021/acscatal.7b02649

Giglio, E., Pirone, R., Bensaid, S., 2021a. Dynamic modelling of methanation reactors during start-up and regulation in intermittent power-to-gas applications. Renew. Energy 170, 1040–1051. https://doi.org/10.1016/J.RENENE.2021.01.153

Giglio, E., Vitale, G., Lanzini, A., Santarelli, M., 2021b. Integration between biomass gasification and high-temperature electrolysis for synthetic methane production. Biomass-.-. Bioenergy 148. https://doi.org/10.1016/J.BIOMBIOE.2021.106017

Grosvenor, A.P., Kobe, B.A., Biesinger, M.C., McIntyre, N.S., 2004. Investigation of multiplet splitting of Fe 2p XPS spectra and bonding in iron compounds. Surf. Interface Anal. 36, 1564–1574. https://doi.org/10.1002/SIA.1984

Guo, L., Sun, J., Ji, X., Wei, J., Wen, Z., Yao, R., Xu, H., Ge, Q., 2018. Directly converting carbon dioxide to linear α-olefins on bio-promoted catalysts. Commun. Chem. https://doi.org/10.1038/s42004-018-0012-4

Guzmán, H., Salomone, F., Batuecas, E., Tommasi, T., Russo, N., Bensaid, S., Hernández, S., 2021. How to make sustainable CO_2 conversion to Methanol: Thermocatalytic versus electrocatalytic technology. Chem. Eng. J. 417, 127973. https://doi.org/10.1016/J.CEJ.2020.127973

Guzmán, H., Salomone, F., Bensaid, S., Castellino, M., Russo, N., Hernández, S., 2022. CO2Conversion to Alcohols over Cu/ZnO Catalysts: Prospective Synergies between Electrocatalytic and Thermocatalytic Routes. ACS Appl. Mater. Interfaces 14, 517–530. https://doi.org/10.1021/acsami.1c15871

Jiang, Y., Wang, K., Wang, Y., Liu, Z., Gao, X., Zhang, J., Ma, Q., Fan, S., Zhao, T.S., Yao, M., 2023. Recent advances in thermocatalytic hydrogenation of carbon dioxide to light olefins and liquid fuels via modified Fischer-Tropsch pathway. J. CO_2 Util. 67. https://doi.org/10.1016/J.JCOU.2022.102321

Jin Chae, H., Kim, J.-H., Chool Lee, S., Kim, H.-S., Bin Jo, S., Ryu, J.-H., Young Kim, T., Ho Lee, C., Jeong Kim, S., Kang, S.-H., Chang Kim, J., Park, M.-J., 2020. Catalytic Technologies for CO Hydrogenation for the Production of Light Hydrocarbons and Middle Distillates. Catalysts. https://doi.org/10.3390/catal10010099

Karre, A.V., Kababji, A., Kugler, E.L., Dadyburjor, D.B., 2012. Effect of addition of zeolite to iron-based activated-carbon-supported catalyst for Fischer-Tropsch synthesis in separate beds and mixed beds. Catal. Today 198, 280–288. https://doi.org/10.1016/j.cattod.2012.04.068

Li, J.B., Ma, H.F., Zhang, H.T., Sun, Q.W., Ying, W.Y., Fang, D.Y., 2014. Sodium promoter on iron-based catalyst for direct catalytic synthesis of light alkenes from syngas. Fuel Process. Technol. 125, 119–124. https://doi.org/10.1016/j.fuproc.2014.03.017

Liang, B., Sun, T., Ma, J., Duan, H., Li, L., Yang, X., Zhang, Y., Su, X., Huang, Y., Zhang, T., 2019. Mn decorated Na/Fe catalysts for CO_2 hydrogenation to light olefins. Catal. Sci. Technol. 9, 456–464. https://doi.org/10.1039/c8cy02275e

Lin, T., An, Y., Yu, F., Gong, K., Yu, H., Wang, C., Sun, Y., Zhong, L., 2022. Advances in Selectivity Control for Fischer–Tropsch Synthesis to Fuels and Chemicals with High Carbon Efficiency. ACS Catal. 12092–12112. https://doi.org/10.1021/acscatal.2c03404

Liu, J., Zhang, A., Jiang, X., Liu, M., Zhu, J., Song, C., Guo, X., 2018. Direct transformation of carbon dioxide to value-added hydrocarbons by physical mixtures of Fe_5C_2 and K-modified Al2O3. Ind. Eng. Chem. Res 57, 9120–9126. https://doi.org/10.1021/acs.iecr.8b02017

Ma, G., Xu, Y., Wang, J., Bai, J., Du, Y., Zhang, J., Ding, M., 2020, An Na-modified Fe@C core-shell catalyst for the enhanced production of gasoline-range hydrocarbons via Fischer-Tropsch synthesis †. https://doi.org/10.1039/d0ra01036g.

Marocco, P., Morosanu, E.A., Giglio, E., Ferrero, D., Mebrahtu, C., Lanzini, A., Abate, S., Bensaid, S., Perathoner, S., Santarelli, M., Pirone, R., Centi, G., 2018. CO_2 methanation over Ni/Al hydrotalcite-derived catalyst: Experimental characterization and kinetic study. Fuel 225, 230–242. https://doi.org/10.1016/J.FUEL.2018.03.137

Mazza, A., Salomone, F., Arrigo, F., Bensaid, S., Bompard, E., Chicco, G., 2020. Impact of Power-to-Gas on distribution systems with large renewable energy penetration. Energy Convers. Manag.: X 7, 100053. https://doi.org/10.1016/J.ECMX.2020.100053

Numpilai, T., Cheng, C.K., Limtrakul, J., Witoon, T., 2021. Recent advances in light olefins production from catalytic hydrogenation of carbon dioxide. Process Saf. Environ. Prot. 151, 401–427. https://doi.org/10.1016/J.PSEP.2021.05.025

Ojelade, O.A., Zaman, S.F., 2021. A review on CO_2 hydrogenation to lower olefins: Understanding the structure-property relationships in heterogeneous catalytic systems. J. CO_2 Util. 47, 101506. https://doi.org/10.1016/J.JCOU.2021.101506

Panzone, C., Philippe, R., Chappaz, A., Fongarland, P., Bengaouer, A., 2020. Power-to-Liquid catalytic CO_2 valorization into fuels and chemicals: Focus on the Fischer-Tropsch route. J. CO_2 Util. 38, 314–347. https://doi.org/10.1016/j.jcou.2020.02.009

Parigi, D., Giglio, E., Soto, A., Santarelli, M., 2019. Power-to-fuels through carbon dioxide Re-Utilization and high-temperature electrolysis: A technical and economical comparison between synthetic methanol and methane. J. Clean. Prod. 226, 679–691. https://doi.org/10.1016/J.JCLEPRO.2019.04.087

Perego, C., Bortolo, R., Zennaro, R., 2009. Gas to liquids technologies for natural gas reserves valorization: The Eni experience. Catal. Today 142, 9–16. https://doi.org/10.1016/J.CATTOD.2009.01.006

Porta, A., Falbo, L., Visconti, C.G., Lietti, L., Bassano, C., Deiana, P., 2020. Synthesis of Ru-based catalysts for CO_2 methanation and experimental assessment of intraporous transport limitations. Catal. Today 343, 38–47. https://doi.org/10.1016/J.CATTOD.2019.01.042

Riedel, T., Schulz, H., Schaub, G., Jun, K.-W., Hwang, J.-S., Lee, K.-W., 2003. Fischer–Tropsch on Iron with H_2/CO and H_2 /CO_2 as Synthesis Gases: The Episodes of Formation of the Fischer–Tropsch Regime and Construction of the Catalyst. Top. Catal. 26, 41–54. https://doi.org/10.1023/B:TOCA.0000012986.46680.28

Salomone, F., Bonura, G., Frusteri, F., Castellino, M., Fontana, M., Chiodoni, A.M., Russo, N., Pirone, R., Bensaid, S., 2022. Physico-Chemical Modifications Affecting the Activity and Stability of Cu-Based Hybrid Catalysts during the Direct Hydrogenation of Carbon Dioxide into Dimethyl-Ether. Materials 15, 7774. https://doi.org/10.3390/MA15217774/S1

Salomone, F., Giglio, E., Ferrero, D., Santarelli, M., Pirone, R., Bensaid, S., 2019. Techno-economic modelling of a Power-to-Gas system based on SOEC electrolysis and CO_2 methanation in a RES-based electric grid. Chem. Eng. J. 377, 120233. https://doi.org/10.1016/J.CEJ.2018.10.170

Salomone, F., Marocco, P., Ferrario, D., Lanzini, A., Fino, D., Bensaid, S., Santarelli, M., 2023a. Process simulation and energy analysis of synthetic natural gas production from water electrolysis and CO_2 capture in a waste incinerator. Appl. Energy 343, 121200. https://doi.org/10.1016/j.apenergy.2023.121200

Salomone, F., Sartoretti, E., Ballauri, S., Castellino, M., Novara, C., Giorgis, F., Pirone, R., Bensaid, S., 2023b. CO_2 hydrogenation to methanol over Zr- and Ce-doped indium oxide. Catal. Today 423, 114023. https://doi.org/10.1016/J.CATTOD.2023.01.030

Scanlon, J.T., Willis, D.E., 1985. Calculation of flame ionization detector relative response factors using the effective carbon number concept. J. Chromatogr. Sci. 23, 333–340. https://doi.org/10.1093/chromsci/23.8.333

Serrano, D.P., Aguado, J., Escola, J.M., Rodriguez, J.M., Peral, A., 2008. Effect of the organic moiety nature on the synthesis of hierarchical ZSM-5 from silanized protozeolitic units. J. Mater. Chem. 18, 4210–4218. https://doi.org/10.1039/b805502e

Sharma, P., Sebastian, J., Ghosh, S., Creaser, D., Olsson, L., 2021. Recent advances in hydrogenation of CO_2 into hydrocarbonsviamethanol intermediate over heterogeneous catalysts. Catal. Sci. Technol. 11, 1665–1697. https://doi.org/10.1039/d0cy01913e

Song, F., Yong, X., Wu, X., Zhang, W., Ma, Q., Zhao, T., Tan, M., Guo, Z., Zhao, H., Yang, G., Tsubaki, N., Tan, Y., 2022. FeMn@HZSM-5 capsule catalyst for light olefins direct synthesis via Fischer-Tropsch synthesis: Studies on depressing the CO_2 formation. Appl. Catal. B 300, 120713. https://doi.org/10.1016/j.apcatb.2021.120713

Wang, D., Xie, Z., Porosoff, M.D., Chen, J.G., 2021. Recent advances in carbon dioxide hydrogenation to produce olefins and aromatics. Chem 7, 2277–2311. https://doi.org/10.1016/j.chempr.2021.02.024

Wang, Y., Kazumi, S., Gao, W., Gao, X., Li, H., Guo, X., Yoneyama, Y., Yang, G., Tsubaki, N., 2020. Direct conversion of CO_2 to aromatics with high yield via a modified Fischer-Tropsch synthesis pathway. Appl. Catal. B 269, 118792. https://doi.org/10.1016/j.apcatb.2020.118792

Wang, Y., Tan, L., Tan, M., Zhang, P., Fang, Y., Yoneyama, Y., Yang, G., Tsubaki, N., 2019. Rationally designing bifunctional catalysts as an efficient strategy to boost CO_2 hydrogenation producing value-added aromatics. ACS Catal. 9, 895–901. https://doi.org/10.1021/acscatal.8b01344

Weber, J.L., Dugulan, I., de Jongh, P.E., de Jong, K.P., 2018. Bifunctional catalysis for the conversion of synthesis gas to olefins and aromatics. ChemCatChem 10, 1107–1112. https://doi.org/10.1002/cctc.201701667

Weber, J.L., Krans, N.A., Hofmann, J.P., Hensen, E.J.M., Zecevic, J., de Jongh, P.E., de Jong, K.P., 2020. Effect of proximity and support material on deactivation of bifunctional catalysts for the conversion of synthesis gas to olefins and aromatics. Catal. Today 342, 161–166. https://doi.org/10.1016/j.cattod.2019.02.002

Wei, J., Ge, Q., Yao, R., Wen, Z., Fang, C., Guo, L., Xu, H., Sun, J., 2017. Directly converting CO_2 into a gasoline fuel. Nat. Commun. 8, 15174. https://doi.org/10.1038/ncomms15174

Wei, J., Sun, J., Wen, Z., Fang, C., Ge, Q., Xu, H., 2016. New insights into the effect of sodium on Fe3O4- based nanocatalysts for CO_2 hydrogenation to light olefins. Catal. Sci. Technol. 6, 4786–4793. https://doi.org/10.1039/c6cy00160b

Wei, J., Yao, R., Ge, Q., Wen, Z., Ji, X., Fang, C., Zhang, J., Xu, H., Sun, J., 2018, Catalytic Hydrogenation of CO_2 to Isoparaffins over Fe-Based Multifunctional Catalysts. https://doi.org/10.1021/acscatal.8b02267.

Wei, J., Yao, R., Ge, Q., Xu, D., Fang, C., Zhang, J., Xu, H., Sun, J., 2021. Precisely regulating Brønsted acid sites to promote the synthesis of light aromatics via CO_2 hydrogenation. Appl. Catal. B 283, 119648. https://doi.org/10.1016/J.APCATB.2020.119648

Wen, C., Jiang, J., Chiliu, C., Tian, Z., Xu, X., Wu, J., Wang, C., Ma, L., 2020. Single-Step Selective Conversion of Carbon Dioxide to Aromatics over Na-Fe_3O_4/Hierarchical HZSM-5 Zeolite Catalyst. Energy Fuels 34, 11282–11289. https://doi.org/10.1021/acs.energyfuels.0c02120

Xu, Y., Liu, D., Liu, X., 2018, Conversion of syngas toward aromatics over hybrid Fe-based Fischer-Tropsch catalysts and HZSM-5 zeolites. https://doi.org/10.1016/j.apcata.2018.01.012.

Xu, Y., Shi, C., Liu, B., Wang, T., Zheng, J., Li, W., Liu, D., Liu, X., 2019. Selective production of aromatics from CO 2. Catal. Sci. Technol. 9, 593–610. https://doi.org/10.1039/c8cy02024h

Xu, Y., Wang, T., Shi, C., Liu, B., Jiang, F., Liu, X., 2020. Experimental Investigation on the Two-Sided Effect of Acidic HZSM-5 on the Catalytic Performance of Composite Fe-Based Fischer-Tropsch Catalysts and HZSM-5 Zeolite in the Production of Aromatics from CO_2/H2. Ind. Eng. Chem. Res 59, 8581–8591. https://doi.org/10.1021/acs.iecr.0c00992

Yang, Q., Kondratenko, V.A., Petrov, S.A., Doronkin, D.E., Saraçi, E., Lund, H., Arinchtein, A., Kraehnert, R., Skrypnik, A.S., Matvienko, A.A., Kondratenko, E.V., 2022. Identifying Performance Descriptors in CO_2 Hydrogenation over Iron-Based Catalysts Promoted with Alkali Metals. Angew. Chem. - Int. Ed. https://doi.org/10.1002/ANIE.202116517

Yang, Q., Skrypnik, A., Matvienko, A., Lund, H., Holena, M., Kondratenko, E.V., 2021. Revealing property-performance relationships for efficient CO_2 hydrogenation to higher hydrocarbons over Fe-based catalysts: Statistical analysis of literature data and its experimental validation. Appl. Catal. B 282, 119554. https://doi.org/10.1016/j.apcatb.2020.119554

Zhang, Z., Liu, Y., Jia, L., Sun, C., Chen, B., Liu, R., Tan, Y., Tu, W., 2022. Effects of the reducing gas atmosphere on performance of FeCeNa catalyst for the hydrogenation of CO_2 to olefins. Chem. Eng. J. 428, 1385–8947. https://doi.org/10.1016/j.cej.2021.131388

Zhong, Y., Mao, Y., Shi, S., Wan, M., Ma, C., Wang, S., Chen, C., Zhao, D., Zhang, N., 2019. Fabrication of magnetic Pd/MOF hollow nanospheres with double-shell structure: toward highly efficient and recyclable nanocatalysts for hydrogenation reaction. ACS Appl. Mater. Interfaces 11, 32251–32260. https://doi.org/10.1021/acsami.9b07864